

Ground states and vortices of matter-wave condensates and optical guided waves

Tristram J. Alexander¹ and Luc Bergé²

¹*Nonlinear Physics Group, Research School of Physical Sciences and Engineering, Australian National University, Canberra ACT 0200, Australia*

²*Département de Physique Théorique et Appliquée, Commissariat à l'Energie Atomique, CEA-DAM/Ile de France, Boîte Postale-12, F-91680 Bruyères-le-Châtel, France*

(Received 26 June 2001; revised manuscript received 2 October 2001; published 25 January 2002)

We analyze the shape and stability of localized states in nonlinear cubic media with space-dependent potentials modeling an inhomogeneity. By means of a static variational approach, we describe the ground states and vortexlike stationary solutions, either in dilute atom gases or in optical cavities, with an emphasis on parabolic-type potentials. First, we determine the existence conditions for soliton and vortex structures for both focusing and defocusing nonlinearity. It is shown that, even for a defocusing medium, soliton modes can exist with a confining potential. Second, step potentials and boundedness effects in hollow capillaries are investigated, which both proceed from a similar analysis. Finally, we discuss applications of this procedure to charged vortices in dilute quantum gases and to Bose-Einstein condensates trapped in the presence of a light-induced Gaussian barrier.

DOI: 10.1103/PhysRevE.65.026611

PACS number(s): 42.65.Tg, 03.75.Fi, 03.65.Ge, 05.30.Jp

I. INTRODUCTION

Excitations described by the nonlinear Schrödinger (NLS) equation and by the Gross-Pitaevskii (GP) equation have attracted significant interest during recent years. Their behavior under the influence of spatial inhomogeneities is now the scope of intensive investigations. On the one hand, the NLS equation including space-dependent potentials currently models the slowly varying complex envelope of waves evolving in a dispersive nonlinear medium with a density profile. It applies, for instance, to light beams trapped in waveguides with graded index [1,2], to the optical Kerr self-focusing in a parabolic medium [3], and to molecular excitations in the vicinity of impurities [4]. For an optical focusing medium, it is expected that the beam can relax to a stable solitary-wave structure, usually called “soliton,” which is the nodeless, ground-state solution of the NLS equation [5]. These states are then stable if their power integral (L^2 norm) does not exceed the critical threshold for self-focusing, and if the variation of this integral versus the soliton parameter is positive [6–8]. Otherwise, they collapse at a finite distance by diverging in amplitude [3,9–14]. Close to this property is the behavior of light beams in hollow capillary waveguides. In this context, the potential does not follow from spatial variations in the density profile, but from appropriate boundary conditions. By imposing the beam envelope to be zero beyond the core radius of the capillary [15–18], a robust waveguide can form and propagate along several Rayleigh lengths in the capillary. On the other hand, the GP equation provides a model equation for describing the collective dynamics of Bose-Einstein condensates (BEC) in ultracold atomic gases [19–24]. This equation is nothing else but the NLS equation supplemented by a quadratic-in-space potential related to the magnetic trap. When bosons undergo attractive interactions—which induce a focusing nonlinearity in, e.g., Li atom gases—the macroscopic wave function of the condensate collapses, as the mean number of particles exceeds a critical value again [21]. Otherwise it may relax to

a stable, stationary object described by the stationary modes of the GP equation. In that case, a criterion of stability for BEC ground states is given by the derivative of the number of bosonic particles with respect to their chemical potential. This derivative must be negative [22,24].

On the basis of these results, we can already observe how the dynamics of nonlinear light beams propagating in a cubic medium with a density profile is close to that of BECs confined by a magnetic trap. From this resemblance, it was recently proposed that a “photon fluid” could behave as a superfluid having a Bogoliubov-type dispersion relation, capable of forming stable two-dimensional (2D) condensates of light in appropriate media [25]. Briefly speaking, photons behave as bosons and they may condense in atom vapors. Superfluidity of photons could be brought to light by means of an incident plane wave traversing a nonlinear medium inside a Fabry-Pérot cavity with a cylindrical obstacle [26]. A strong single moding in a cylindrical Fabry-Pérot resonator filled with atomic Rb vapor was already reported in Ref. [27].

From the pioneering work [5] that displayed the existence of the so-called Townes modes, many works have been devoted to find, at least numerically, these elementary soliton-like excitations and to test their stability. Townes modes, i.e., “bright” localized solitons, are not the only candidates for supporting condensate distributions. For a defocusing medium with no external potential, we already know that no localized solution exists and such media only promote delocalized travelling-wave solutions named dark solitons [28,29]. However, we shall here show that, in the presence of a confining potential, “bright” solitons also exist for a defocusing medium. Furthermore, localized vortex modes carrying an orbital angular momentum can arise as elementary solutions to the 2D NLS equation. These structures do not possess the radial symmetry in general. They exhibit a ring-shaped field distribution with a rotating spiral character related to the azimuthal angle. In the absence of a trap, existence conditions for such objects have been established in

Ref. [30] in the scope of nonlinear optics. In this context, it was numerically discovered and proven that, although stable against radial perturbations, ringlike (vortexlike) modes in saturable focusing media are unstable against azimuthal perturbations and they can decay into $2|m|$ nodeless solitons, where m denotes the azimuthal index (“charge”) number [31,32]. With a parabolic-type potential, similar modes may exist. At lowest order, some of them are radially symmetric ($m=0$), which have numerically been identified in Ref. [22]. Let us recall that these different structures can mutually interact. For instance, experiments showing the attraction and fusion of 3D bright spatial solitons resulting from the modulational instability of an optical vortex have been reported in Ref. [33] for saturable focusing rubidium vapors. Besides, the decay of vortices with high “charge” number m into an aligned array of m vortices of unit charge that repel each other has been experimentally realized in anisotropic, photorefractive crystals [34]. In the same material, two initially round Gaussian beams were moreover observed to converge towards bound dipole solitary solutions [35]. Defocusing media favoring the formation and the interaction of dark solitons have been extensively studied from the experimental point of view, which the interested reader can find reviewed in Ref. [36].

Analogous structures can also be produced in confined quantum gases. In Ref. [37], the properties of the ground stationary states of BECs were determined by means of variational arguments and the validity of the Thomas-Fermi approximation, neglecting the kinetic energy of the condensate for large particle numbers, was justified. In addition, vortex lines with closed path and phase undergoing 2π winding were expected to be triggered by rotation of the trap, with an angular momentum above a critical value [37]. For repulsive interactions, excitations of vortex states have been classified in Ref. [38] and their stability has been investigated in Refs. [39–42], within and beyond the Thomas-Fermi approximation. Through minimization principles applied to the energy functional, it was shown [40,41] that at zero temperature a quantum vortex with lowest possible circulation (i.e., with charge number equal to unity) should be stable, whereas higher-order vortices with $|m| > 1$ should undergo instability. In particular, vortex with, e.g., $m=2$ can split into two distinct vortices with $|m|=1$, symmetrically dispatched. A rotating trap may, however, stabilize the system [39], and at finite temperature a singly charged vortex can only decay in the presence of dissipation [42]. Note that vortex stability was mainly studied for condensates with repulsive interactions, apart from a perturbative treatment [41], which predicts stability of the single vortex state with weak attractive interaction and instability of higher-order modes. Stability of quantum vortices with attractive interaction thus deserves numerical confirmation, which we address in the forthcoming analysis.

Quite recently, vortices have been experimentally created in ^{87}Rb atom gases following two distinct methods. The first method [43] uses a combination of a laser and a microwave field to print the desired velocity field onto the atomic wave function, which generates a condensate rotating around a second, stationary one. The second method [44] superim-

poses onto the magnetic potential a nonaxisymmetric, dipole potential created by a stirring laser beam. The combined potential leads to a cigar-shaped harmonic trap with anisotropic transverse profile, which is rotated and allows for vortex nucleation. With the latter setup, up to four vortices have been produced at fast enough rotation frequencies. Observation of scissors modes, excited by a sudden rotation of the anisotropic trap, has also been reported in similar media [45]. Let us recall again that these different basic structures may mutually interact and evolve into each other, as in optical bulk materials. For instance, the interaction of a trapped ground state and a vortex has numerically been shown to give rise to fringe patterns [46]. A phase slip in the fringes of the interference pattern characterizes the vorticity, which was proposed as a sure diagnostic for detecting vortices in Bose-Einstein condensates. Dislocation in the fringe pattern, that gives the signature of the presence of vortices nucleated by laser stirring, have been experimentally measured in Ref. [47]. Vortices can also emerge from the flow of an object through a dilute Bose-Einstein condensate trapped in a harmonic well [48]. The BEC wave function is then modeled by the 2D GP equation with a Gaussian barrier that describes a macroscopic “light-induced obstacle.” This model can serve for proving the superfluid nature of the condensate, where strong dissipation arises when the relative velocity between the object and the fluid exceeds a critical value proportional to the speed of sound. The superfluid flow then becomes unstable against the formation of vortex pairs with opposite circulation, which signals the onset of a new, dissipative regime. This property has been verified experimentally [49], when the macroscopic object was simulated by a blue detuned laser beam repelling atoms from its focus. The same experimental setup also allowed for displaying evidence of a critical velocity for the onset of a drag force between the laser beam and the condensate. These properties were earlier numerically predicted in Ref. [50] for superfluids having a defocusing (repulsive) nonlinearity and no trap. It is important to recall that Landau theory for a critical velocity below which a superfluid evolves without dissipation basically concerns microscopic objects, instead of macroscopic ones. To prove superfluidity of BECs in this sense, impurity atoms were used in [51]. It was observed that collisions between impurity and the stationary condensate were significantly reduced with impurity velocities below the condensate speed of sound, in agreement with the Landau criterion for superfluidity. By comparison with nonlinear optical media, we finally mention that quasi-1D dark solitons have also been experimentally created in cigar-shaped BECs of ^{87}Rb by a phase imprinting method [52]. Detailed comparison of experimental data with theory and numerical simulations [53] allowed for identifying dark solitons travelling with almost constant velocity smaller than the speed of sound.

In view of the above results, the key point is to identify which kind of steady-state/stationary structure can serve as an attractor providing a stable nonlinear mode, that could sustain a long-living condensate. This issue cannot be cleared up through extensive numerical simulations only. We need a way to determine analytically the characteristic length and amplitude of such steady-state modes. Therefore, this

paper is aimed at proposing a systematic procedure for finding the approximate shapes of soliton and vortex solutions of the NLS equation

$$i\partial_t\psi + \nabla^2\psi + \sigma|\psi|^2\psi - U(\vec{r})\psi = 0, \quad (1)$$

where ψ denotes either a macroscopic BEC wave function evolving in time (in which case t is a time variable), or the slowly varying envelope of a nonlinear light field propagating in an inhomogeneous Kerr medium (in which case t refers to a propagation variable). The Laplacian ∇^2 expresses in spherical geometry as $\nabla^2 = r^{1-D}\partial_r r^{D-1}\partial_r$ with space dimension number D . In 2D ($D=2$), we shall examine vortex solutions for which $\nabla^2 = r^{-1}\partial_r r\partial_r + r^{-2}\partial_\theta^2$, θ being the azimuthal angle. In Eq. (1), σ is the nonlinearity coefficient that is positive (negative) for attractive (repulsive) interactions between bosons or for a focusing (defocusing) optical medium. $U(\vec{r})$ represents a space-dependent potential. For the sake of simplicity, we shall restrict our analysis to localized nonlinear modes decaying to zero at infinity and assume that the potential U always preserves their initial centroid.

The paper is organized as follows: Sec. II provides some general existence conditions for the localized stationary nonlinear modes of Eq. (1). It also expounds a static variational approach, which describes the shape, amplitude, and radius of discrete NLS modes. Emphasis is then given to a parabolic profile $U(\vec{r}) \sim r^2$ in Sec. III. For this case, the time evolution of solutions revealed in, e.g., Ref. [13] are refound and generalized for any test function. Their stationary version then supplies the soliton modes, $\psi(\vec{r}, t) = \phi(\vec{r})e^{i\lambda t}$, whose characteristic integrals vary with the parameter λ . These variations, estimated analytically, are shown to be in remarkable agreement with direct numerical computations. For $D=2$, Sec. IV presents similar results for a step potential $U(\vec{r}) = -\epsilon H(R-r)$, where H is the usual Heaviside function, ϵ and $2R$ are the height and diameter of the potential, respectively. In Sec. V, we propose an analogy with hollow capillary waveguides, whose spatial effects originate from appropriate boundary conditions, such as $\psi(|\vec{r}| \geq R) = 0$. In that case and for a step potential as well, we numerically verify that the same criterion for soliton stability holds. Vortexlike solutions carrying an angular orbital momentum are next studied in Sec. VI for both cases $\sigma = \pm 1$, by means of the same variational procedure. Their stability is numerically tested and thoroughly discussed for attractive interactions. Finally, we apply our analytical method to the BEC ground states interacting with an external Gaussian obstacle, as modeled in Ref. [48].

II. GENERAL RESULTS

A. Existence conditions for localized discrete eigenmodes

We determine the conditions for the existence of both stationary and travelling-wave solutions of Eq. (1), expressed in the canonical form

$$\psi(\vec{r}, t) = \phi(\vec{r} - \vec{v}t, \lambda)e^{i\lambda t}, \quad (2)$$

with velocity \vec{v} and soliton parameter λ . Here, all functions ϕ are assumed to be localized in space with $\phi \rightarrow 0$ as

$r \rightarrow +\infty$ and all spatial derivatives of ϕ vanish at boundaries. In these conditions, ϕ obeys the differential equation

$$-\lambda\phi - i\vec{v} \cdot \vec{\nabla}\phi + \nabla^2\phi + \sigma|\phi|^2\phi - U(\vec{r})\phi = 0. \quad (3)$$

For further convenience, we emphasize that the eigenmode ϕ realizes a critical point ($\delta S = 0$) for the general functional

$$S = H + \lambda N - \vec{v} \cdot \vec{P}, \quad (4)$$

where

$$N \equiv \int |\psi|^2 d\vec{r} \quad (5)$$

is the power integral or number of particles for Eq. (1);

$$H \equiv \int \left\{ |\vec{\nabla}\psi|^2 - \frac{\sigma}{2} |\psi|^4 + U(\vec{r})|\psi|^2 \right\} d\vec{r} \quad (6)$$

is the Hamiltonian which is conservative for real-valued potentials U , and

$$\vec{P} \equiv \frac{i}{2} \int (\psi \vec{\nabla}\psi^* - \psi^* \vec{\nabla}\psi) d\vec{r} \quad (7)$$

is the linear transverse momentum (* means complex conjugate). Three particular modes can then be investigated, namely:

(i) The ground states (GS), being positive, nodeless, radially symmetric with maximum located at $\vec{r} = \vec{0}$, and possessing no velocity. This leads us to set $\vec{v} = \vec{0}$ and $\nabla^2 = r^{1-D}\partial_r r^{D-1}\partial_r$ in Eq. (3). Such modes arise in the field of nonlinear optics and Bose-Einstein condensations as well, as the most elementary solution serving as a ‘‘bright’’ soliton. They constitute critical points for the variational problem $\delta(H + \lambda N) = 0$ resolved at fixed number $N = N_s \equiv \int |\phi|^2 d\vec{r}$. *For a focusing medium, GS are generally stable whenever the derivative $dN/d\lambda$, with $N = N_s$, is positive, and when the curvature of the potential U is positive around the soliton centroid [6]. They must also satisfy $N_s < N_c$ to avoid collapse.*

(ii) The travelling-wave solutions (TWS) being the analogous of the previous modes, but they carry a nonzero velocity $\vec{v} \neq \vec{0}$ and propagate inside the medium. They are characterized by a nonzero transverse momentum \vec{P} and solve the variational problem $\delta(H - \vec{v} \cdot \vec{P}) = 0$. In 1D a stability criterion for such structures may be given by $dP/dv < 0$, at least for dark solitons [28,29]. Travelling-wave solutions will not be thoroughly investigated in the present analysis, except along the following general discussion.

(iii) The vortex solutions (VS) [60,32] having the form $\phi(\vec{r} - \vec{v}t) = \chi(\vec{r}, \vec{v})e^{im\theta}$ with azimuthal angle θ and model index m . They possess a nonzero angular momentum $\vec{L} \equiv \int d\vec{r}(\vec{r} \times \vec{p})$ where \vec{p} is the density of the transverse momentum (7). For the sake of simplicity, we shall restrict the analysis of such objects to two-dimensional structures ($D = 2$) with no velocity ($\vec{v} = \vec{0}$). These states then obey \vec{P}

$=\vec{0}$ and $|\vec{L}|=|m|\theta$. They exhibit a ring shape, i.e., they are zero at center and reach a maximum at a nonzero transverse coordinate, while they possess a constant orbital motion. Their radial profile χ is governed by Eq. (3), in which the two-dimensional Laplacian operator must be replaced by $\nabla^2=r^{-1}\partial_r r\partial_r-m^2/r^2$.

To start with, we consider Eq. (3) for any arbitrary number D and potential U . On the one hand, we multiply it by ϕ^* and integrate the result in the whole spatial domain to find

$$-\lambda N + \vec{v} \cdot \vec{P} - \int |\vec{\nabla} \phi|^2 d\vec{r} + \sigma \int |\phi|^4 d\vec{r} - \int U |\phi|^2 d\vec{r} = 0. \quad (8)$$

On the other hand, after multiplying Eq. (3) by $\vec{r} \cdot \vec{\nabla} \phi^*$, selecting the real part of the result and integrating over space, we obtain

$$D\lambda N - \frac{D\sigma}{2} \int |\phi|^4 d\vec{r} - \int U \vec{r} \cdot \vec{\nabla} |\phi|^2 d\vec{r} + (D-2) \int |\vec{\nabla} \phi|^2 d\vec{r} - (D-1) \vec{v} \cdot \vec{P} = 0. \quad (9)$$

Combining the two relations (8) and (9) then yields

$$\vec{v} \cdot \vec{P} - 2 \int |\vec{\nabla} \phi|^2 d\vec{r} + \frac{\sigma D}{2} \int |\phi|^4 d\vec{r} + \int |\phi|^2 \vec{r} \cdot \vec{\nabla} U d\vec{r} = 0. \quad (10)$$

Note that when we apply the above relations to vortex solutions, we have to express the terms $\vec{r} \cdot \vec{\nabla} |\phi|^2$ and $|\vec{\nabla} \phi|^2$ in the integrands as $r\partial_r |\chi|^2$ and $|\partial_r \chi|^2 + m^2 |\chi|^2 / r^2$, respectively. Equations (8) to (10) are quite instructive and lead us to list the following properties:

With $U=0$, ground state, travelling wave, and vortex solutions can exist for attractive, focusing media ($\sigma>0$). In particular, GS and VS modes with no velocity make sense for $\lambda>0$ only. In the repulsive, defocusing case ($\sigma<0$), neither of these modes exist, even for negative λ 's.

With $U\neq 0$, the previous constraints can be relieved to some extent, depending on the spatial shape of the potential. Because we mainly focus on parabolic inhomogeneities, we shall comment on potentials of the form $U=\Omega_0^2 r^2/4$, where Ω_0 is related to the trap frequency [4,22,24]. In this context, the important result follows: For a defocusing medium ($\sigma<0$), *both ground states and vortices can exist whenever*

$$\Omega_0^2 \int r^2 |\phi|^2 d\vec{r} > |\sigma| D \int |\phi|^4 d\vec{r}. \quad (11)$$

This inequality means that these nonlinear modes exist if the confining trap dominates over the nonlinearity.

B. The variational procedure

We now elaborate on a variational principle, inspired by Anderson, Bonnedal, and Lisak [54], in order to approximate the characteristic shape, length and amplitude of the station-

ary modes. With this aim, we follow the basic steps of a variational method, i.e., we use the functional (4), in which we insert an appropriate function. More precisely, we employ

$$\mathcal{S}_\phi \equiv \int \left\{ |\vec{\nabla} \phi|^2 - \frac{\sigma}{2} |\phi|^4 + U(\vec{r}) |\phi|^2 \right\} d\vec{r} + \lambda \int |\phi|^2 d\vec{r} - \vec{v} \cdot \vec{P}_\phi, \quad (12)$$

where \vec{P}_ϕ means the transverse momentum for TWS. When velocity v is zero, we plug into Eq. (12) the trial function $\phi=A\phi_a(r/a)$ with test function ϕ_a , amplitude A and width a . This transforms the above functional into

$$\mathcal{S}_a = \alpha A^2 a^{D-2} - \beta A^4 a^D + A^2 a^D \int U(\vec{\xi}) |\phi_a|^2 d\vec{\xi} + \lambda \delta A^2 a^D, \quad (13)$$

where $\vec{\xi} \equiv \vec{r}/a$, and the integral coefficients read

$$\alpha = \int |\nabla_\xi \phi_a|^2 d\vec{\xi}, \quad \beta = \frac{\sigma}{2} \int |\phi_a|^4 d\vec{\xi}, \quad \delta = \int |\phi_a|^2 d\vec{\xi}. \quad (14)$$

For TWS, the argument in the trial function has to be extended to the generalized variable $(\vec{r}-\vec{v}t)/a$. For vortices (VS) with no velocity, the same step in the procedure applies. The main changes occur within the shape of the test function ϕ_a , which will be commented on below. The second step consists in performing the differentiations

$$\partial \mathcal{S}_a / \partial a = \partial \mathcal{S}_a / \partial A = 0. \quad (15)$$

By doing so, we get the equations for the amplitude and width of the steady-state modes, expressed as functions of the soliton frequency λ . The constraint of a positive power $N=\delta A^2 a^D$ then yields some restrictions on the range of λ , for which localized modes exist. This relation finally provides the variation curve $N=N_s$ vs λ , from which, by applying the stability criterion $dN/d\lambda>0$, we access the stability regions of the nonlinear modes.

Let us now discuss the choice of a suitable candidate for the test function ϕ_a . For single-humped solitons, ϕ_a can be chosen among current functions. GS modes may indeed be modeled by Gaussian shapes, $\phi_a = \exp(-\xi^2/2)$, which present several advantages. First, they are technically convenient to track with and related integral coefficients are, e.g., in 2D: $\alpha = \delta = \pi$ while $\beta = \sigma\pi/4$. In 3D, we have $\alpha = 3\delta/2$, $\beta = \sigma\delta^2/2(2\pi)^{3/2}$ where $\delta = \pi^{3/2}$. Second, up to a relative margin less than 10%, their power integral $N_c^{\text{Gauss}} = 4\pi$ is close to the minimum threshold for collapse with $\sigma = +1$, $N_c \approx 11.7$ [55]. Third, in the special case of a parabolic potential $U \sim r^2$, soliton modes exhibit Gaussian tails, i.e., Gaussians are exact solutions of Eq. (3) in the limit $\sigma \rightarrow 0$, whatever the sign of σ may be. Gaussians thus appear to be suitable candidates, when the contribution from the potential in the GS mode is expected to dominate over the nonlinearity, as emphasized by Eq. (11). Alternatively, we may choose the ground-state solutions of the untrapped NLS equation,

given by Eq. (3) when $U=0$. For $\lambda>0$, it has the symmetry $\phi(r,\lambda)=\sqrt{\lambda}\phi_0(\sqrt{\lambda}r)$ that reduces λ to the unity. Taking ϕ_0 as test function leads to the integral coefficients $\alpha=\delta=N_c$, $\beta=\sigma N_c$ for $D=2$, and $\delta=N_c\approx 18.9$, $\alpha=3N_c$, $\beta=2\sigma N_c$ for $D=3$ (see, e.g., Refs. [56,57]). We recall that the free NLS ground-state mode can be approximated in turn by sech test functions [54,58]. As special attention will be paid on parabolic inhomogeneities, the functional S_a will depend on potential integrals as $\int U(\vec{\xi})|\phi_a|^2 d\vec{\xi}=(\Omega_0^2/4)a^2\gamma$, where

$$\gamma\equiv\int\xi^2|\phi_a|^2 d\vec{\xi} \quad (16)$$

takes the value $\pi(3\pi^{3/2}/2)$ for 2D (3D) Gaussians or $8\pi\times 0.55(20.312)$ for the 2D (3D) free GS test function ϕ_0 .

Furthermore, we shall apply our variational procedure to the identification of single vortex solutions. Their radial profiles are characterized by a minimum at center [$\phi(0)=0$], whereas they exhibit one maximum at a finite radius r . Looking for the asymptotics of solutions ϕ in the form $\phi=\chi(r)e^{im\theta}$ in Eq. (3) with a parabolic potential, we observe that the radial component χ behaves as $r^{|m|}$ near $r=0$ and as the Gaussian $e^{-\Omega_0 r^2/4}$ at large distances. We shall, therefore, select the class of trial functions $\chi=A_m\chi_{a,m}(r/a_m)$ with

$$\chi_{a,m}(\xi)=\frac{\xi^{|m|}}{(B_m+\xi)^{|m|}}e^{-\xi^2/2}, \quad \xi\equiv r/a_m, \quad (17)$$

where A_m , B_m , and a_m are positive Lagrange parameters for fixed azimuthal index m .

III. PARABOLIC INHOMOGENEITIES

Parabolic density profiles are widespread in physics. They can indeed be found in the field of nonlinear excitations with impurities [4], when an exponential trapping, $U(r)=-\epsilon\exp(-r^2/r_0^2)$, reduces to $U(r)\approx\epsilon(r^2/r_0^2-1)$ for a radius of the impurity core, r_0 , much larger than the soliton width. Parabolic inhomogeneities are also met in plasma physics [3] and in nonlinear optics [2], when the plasma density profile or a graded-index optical medium varies parabolically along one privileged direction. In BEC physics, a spatially quadratic potential is naturally provided by the confining trap in dilute atom gases [20]. Keeping in mind this wide range of applicability, we first examine the action of a parabolic potential, $U(r)=\Omega_0^2 r^2/4$, with trap frequency Ω_0 , from both the dynamic and stationary viewpoints. The centroid of the beam, $\vec{R}(t)\equiv N^{-1}\int\vec{r}|\psi|^2 d\vec{r}$, is known to vary as $\ddot{\vec{R}}+\Omega_0^2\vec{R}=\vec{0}$ [4]. In what follows, we shall consider a beam with zero initial velocity and initially fixed at center, which leads us to set $\vec{R}(t)=\vec{0}$. Centroid motions and their influence on the nonlinear beam dynamics and soliton relaxation can be found studied in, e.g., Refs. [4,10,11].

A. Collapsing wave packets in nonlinear parabolic media

As is already known from optical and BEC literature [12–14,20–22,24], a wave function ψ obeying Eq. (1) with potential $U(r)=\Omega_0^2 r^2/4$ and $\sigma=+1$ is condemned to collapse in finite time when, e.g., its initial datum makes the Hamiltonian H negative. This imposes that the integral N must be above the threshold value N_c . For $N\leq N_c$, the wave function ψ either oscillates with period $2\Omega_0$ [4,13] or it can attain a stationary state, which is orbitally stable if $dN/d\lambda>0$ [24]. Let us briefly perform a time-dependent variational approach depicting these main dynamical aspects. For this purpose, we derive from Eq. (1) the identity for the mean-square radius of ψ (see, e.g., Ref. [9]),

$$\begin{aligned} \frac{1}{4}d_t^2\int r^2|\psi|^2 d\vec{r}=2\int|\vec{\nabla}\psi|^2 d\vec{r}-\frac{\sigma D}{2}\int|\psi|^4 d\vec{r}+\int U(\vec{r}) \\ \times[D+\vec{r}\cdot\vec{\nabla}]|\psi|^2 d\vec{r}, \end{aligned} \quad (18)$$

which is valid for a real-valued potential U . We then introduce the self-similarlike substitution

$$\psi(\vec{r},t)=\frac{\phi(\vec{r}/L(t),\tau)}{L^{D/2}(t)}e^{iS(\vec{r},t)}, \quad (19)$$

with $\tau(t)=\int_0^t du/L^2(u)$ and $S(\vec{r},t)=\lambda\tau-\dot{L}r^2/4L$ (dot means d/dt). Selecting U as parabolic and taking ϕ as exactly self-similar, i.e., $\phi=A\bar{\phi}(\vec{r}/L)$, we find that the time-dependent scale length $L(t)$ of the wave packet is governed by

$$\frac{1}{4}L^3\ddot{L}-\epsilon L^4=\frac{\alpha}{\gamma}\left(1-\frac{D\beta}{2\alpha L^{D-2}}\right), \quad (20)$$

where the integral coefficients α , β , γ follow the same notations as in Eqs. (14) and (16), after changing ϕ_a and a by $\bar{\phi}$ and $L(t)$, respectively. From Eq. (20), it is readily seen that collapse occurs whenever $D\beta>2\alpha L^{D-2}$, which must be satisfied, in particular, by the initial length $L_0\equiv L(t=0)$ for beams with no initial contraction rate ($\dot{L}|_{t=0}=0$). Let us then focus our attention on the 2D case, $D=2$. In this configuration, Eq. (20) is exactly solvable. After defining the ratio N over critical by $\beta/\alpha=N/N_c$, a simple integration of Eq. (20) yields the solution [4]

$$L(t)=\left\{u^2(t)+\frac{4\Delta}{W^2}v^2(t)\right\}^{1/2}, \quad (21)$$

where (u,v) is a fundamental set of solutions to the equation $\ddot{L}+\Omega_0^2 L=0$; W denotes the Wronskian $W=\dot{u}v-u\dot{v}$, and $\Delta\equiv(\alpha/\gamma)[1-N/N_c]$. Selecting initial data with no initial velocity, $\dot{L}|_{t=0}=0$, and introducing the ratio $\Delta_c\equiv L_0^4\Omega_0^2/4$, we find

$$L(t)=\frac{L_0}{\sqrt{2}}\left[\left(1-\frac{\Delta}{\Delta_c}\right)\cos(2\Omega_0 t)+1+\frac{\Delta}{\Delta_c}\right]^{1/2}. \quad (22)$$

This relation provides the characteristic dynamics. When $\Delta > \Delta_c$, which implies $N < N_c$, the solution periodically oscillates with period $2\Omega_0$ and starts by increasing with $\dot{L} > 0$. When $\Delta = \Delta_c$, $L(t)$ is frozen on a stationary fixed point that again satisfies $N < N_c$. When $\Delta < \Delta_c$, either Δ is positive, in which case oscillations still develop by decreasing from L_0 with $\dot{L} < 0$, or Δ is negative, in which case collapse occurs with $L(t) \rightarrow 0$ in finite time. This latter singular evolution requires $N > N_c$. The collapse time is given by $t_c = \Omega_0^{-1} \arctan(\sqrt{-\Delta_c/\Delta})$ and it is always smaller than its counterpart for $\Omega_0 = 0$. These results recover those previously established by Karlsson and co-workers [13], who used a similar variational (averaged-Lagrangian) method applied to a Gaussian test function. Here, we have extended their results to any test function that may be Gaussian, sech, or even given by the GS ϕ_0 of the free NLS equation. In Ref. [4] it was observed in the diffractive/oscillation regime that the choice of a sech test-function, known as the best fit for the free NLS ground state, yielded variational results that were in excellent agreement with direct numerical computations. Choosing $\bar{\phi}$ as the free ground state ϕ_0 , which lines up the critical power for collapse onto its minimal value $N_c = 11.7/\sigma$, should improve this agreement to some extent.

B. Stability of GS modes

The previous analysis emphasizes the possibility of forming a stationary state from initial sizes of wave packets fixed at $L_0 = \sqrt{2/\Omega_0}[(\alpha/\gamma)(1 - N/N_c)]^{1/4}$. This result shows that for appropriate integral N and beam size L_0 , a soliton can form, which, however, does not resolve the question of its stability. For solving this point, it is necessary to apply the criterion $dN/d\lambda > 0$ [6] and, thus, to access the variation of N versus λ . The first question is to identify the link between the soliton size L_0 and the soliton parameter λ , and then to infer the curve $N(\lambda)$ with N computed on the GS mode. In the framework of the free NLS equation, this point is easily cleared up, as a soliton state corresponds to a static trial function with size L_0 being equal to the inverse of the square root of $\lambda > 0$, which also follows from the dilation invariance $\phi \rightarrow \sqrt{\lambda} \phi_0(\sqrt{\lambda} r)$. Nonetheless, this equivalence does not apply to a parabolic potential. To identify the variations of the soliton width with respect to λ in that case, we use the static variational method expounded in Sec. II. Regarding GS modes for the potential $U(r) = \Omega_0^2 r^2/4$, we employ single-humped trial functions $\phi = A \phi_a(r/a)$, so that the functional \mathcal{S}_a [Eq. (13)] explicitly reads

$$\mathcal{S}_a = \alpha A^2 a^{D-2} - \beta A^4 a^D + \frac{\Omega_0^2}{4} \gamma A^2 a^{D+2} + \lambda \delta A^2 a^D. \quad (23)$$

The variational equations (15) of \mathcal{S}_a for the amplitude A and size a yield

$$\frac{\Omega_0^2}{4} \gamma a^4 - (2\beta A^2 - \lambda \delta) a^2 + \alpha = 0, \quad (24)$$

$$\frac{\Omega_0^2}{4} (D+2) \gamma a^4 - D(\beta A^2 - \lambda \delta) a^2 + (D-2)\alpha = 0, \quad (25)$$

respectively. Simple combinations of these equations then enable us to determine

$$A(\lambda) = \left[\frac{2\lambda \delta + 4\alpha/a^2}{\beta(4+D)} \right]^{1/2} = \left[\frac{2\lambda \delta + \Omega_0^2 a^2 \gamma}{\beta(4-D)} \right]^{1/2}, \quad (26)$$

$$a(\lambda) = \left[\frac{2\sqrt{(D\lambda \delta)^2 + \Omega_0^2 \gamma \alpha (D+4)(4-D)} - 2D\lambda \delta}{(D+4)\Omega_0^2 \gamma} \right]^{1/2}. \quad (27)$$

Both soliton amplitude and width are explicit functions of λ . Note in this respect that Eqs. (24) and (25) provide $A \propto \lambda^{1/2}$ and a scales like $\lambda^{-1/2}$ in the limit of no potential $\Omega_0 \rightarrow 0$, which reflects the variations of the soliton width $L_0 = a$ with respect to λ for the free NLS equation. With a parabolic potential, these elementary variations become more tricky. The Hamiltonian H and integral N both computed on the soliton mode indeed express as

$$H_s(\lambda) = \frac{A^2(\lambda) a^D(\lambda)}{4-D} [(D-2)\lambda \delta + \Omega_0^2 a^2 \gamma], \quad (28)$$

$$N_s(\lambda) = A^2(\lambda) a^D(\lambda) \delta = \frac{\delta a^D(\lambda)}{4-D} \left(2\lambda \frac{\delta}{\beta} + \Omega_0^2 a^2 \frac{\gamma}{\beta} \right), \quad (29)$$

where the index “ s ” henceforth means that integrals are calculated on the stationary solution. For $\sigma > 0$, the positiveness of N_s imposes a lower bound in the range of λ , i.e., soliton modes exist, provided that λ does not decrease below a cut-off value, λ^* , given by $A^2(\lambda^*) = 0$, namely,

$$\lambda \geq \lambda^* = -\frac{\Omega_0}{\delta} \sqrt{\alpha \gamma}. \quad (30)$$

In the opposite limit $\lambda \rightarrow +\infty$ and for $D=2$, a^2 behaves as the vanishing ratio $\alpha/\lambda \delta$ and N_s reaches the limit $\delta\alpha/\beta$. For $\sigma = +1$ and Gaussian test functions, we thus find $\lambda^* = -\Omega_0$ and $N_s(\lambda)$ tends to $N_c^{\text{Gauss}} = 4\pi$ at large λ . With test function given by the GS of the free NLS equation, ϕ_0 , we find $\lambda^* = -1.0869\Omega_0$ and $N_s(\lambda)$ tends to the minimum bound for collapse $N_c = 11.7$ as $\lambda \rightarrow +\infty$. For $D=3$, a^2 still vanishes as $(\alpha/3\lambda \delta)$, while asymptotically $N_s(\lambda)$ attains the limit value $(2/\beta)(\alpha/3)^{3/2} \sqrt{\delta/\lambda}$. For Gaussian test functions, $\lambda^* = -3\Omega_0/2$ and $N_s(\lambda) \rightarrow 4\pi^{3/2}/\sqrt{\lambda}$ at large λ . For GS test functions ϕ_0 , $\lambda^* = -1.796\Omega_0$ and $N_s(\lambda) \rightarrow N_c/\sqrt{\lambda}$, where $N_c \approx 18.9$ in 3D. These asymptotics indicate that the soliton size decreases at growing λ , until the effect of the potential becomes negligible for $\lambda \gg 1$ and the GS mode recovers the characteristics of an untrapped NLS soliton. In this limit, $dN_s/d\lambda$ becomes zero for $D=2$ and negative for $D=3$, which leads to soliton instability. For other permitted values of λ , the integral $N_s(\lambda)$ is a monotonically increasing function of λ for $D=2$. For $D=3$, it increases from λ^* to a maximum value N_s^{max} attained at $-0.7 \leq \lambda_{\text{max}} \leq -0.5$, then

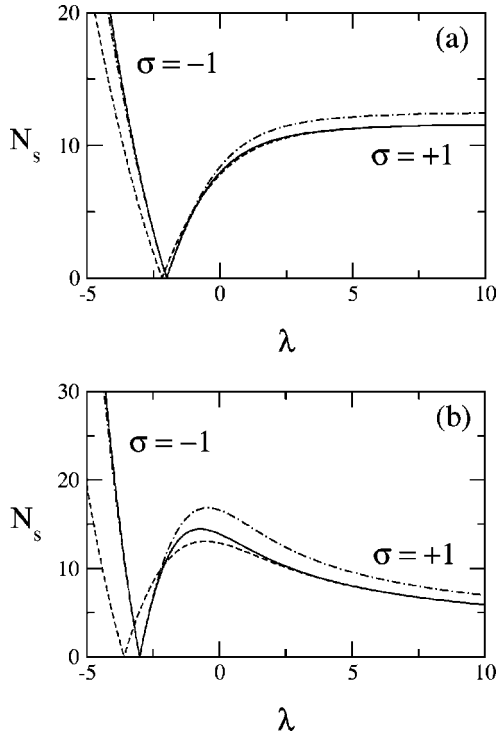


FIG. 1. Soliton mass N_s vs λ determined from direct integrations of Eq. (3) with a parabolic potential (solid curves) and computed from the variational equations involving Gaussian (dash-dotted lines) and the free NLS GS mode (dashed lines) as selected test functions: (a) $D=2$; (b) $D=3$. The left-hand side of the curves refers to a defocusing medium ($\sigma=-1, \lambda < \lambda^*$) and their right-hand side to a focusing medium ($\sigma=+1, \lambda > \lambda^*$).

decreases to zero at larger λ 's. Consequently, all the GS modes are stable for $\lambda \in]\lambda^*, +\infty[$ with $N_s < N_c$ in 2D. They are stable only for λ belonging to the interval $]\lambda^*, \lambda_{\max}[$ and $N_s < N_s^{\max} < N_c$ in 3D.

Figures 1(a) and 1(b) show direct comparisons between the numerically computed soliton modes of Eq. (1) (solid curves) and Eq. (29) computed with Eqs. (26) and (27) for test functions taken as Gaussian (dash-dotted lines) and as the free NLS mode, ϕ_0 (dashed lines). Those are reproduced for $\Omega_0=2$ in the dimensional cases $D=2$ [Fig. 1(a)] and $D=3$ [Fig. 1(b)]. We can observe the good agreement between the variational predictions and the numerics, which emphasizes in particular that 3D soliton modes are stable up to the point $(N_s^{\max}=14.45, \lambda_{\max}=-0.72)$ in the (N_s, λ) plane. Slight discrepancies arise in the values of N_{\max} , at the location of the cut-off λ^* , and in the asymptotics $N_s \rightarrow N_s^{\Omega_0=0} = N_c / \lambda^{(D-2)/2}$ at large λ for Gaussian test functions. Despite these differences, the variational procedure appears to be actually efficient for determining the variations in the soliton size and amplitude with respect to λ , and for identifying the stability regions fixed by the criterion $dN_s/d\lambda > 0$ within a reliable approximation. Note that, with $N_s < N_c$, Eq. (3) has a relatively weak nonlinearity. Gaussian functions in the form $\phi = A e^{-\gamma r^2}$ with constants A , γ thus provide exact solutions of Eq. (3) in the limit $\sigma \rightarrow 0$, whenever $\gamma = \Omega_0/4 = -\lambda/2D$, which yields the cut-off parameter

λ^* . This partly justifies why Gaussians are trustworthy candidates in the variational approach.

For a defocusing medium ($\sigma = -1$), $A^2(\lambda) > 0$ makes sense for the inequality opposite to Eq. (30), $\lambda \leq \lambda^* = -(\Omega_0/\delta)\sqrt{\alpha}\gamma$. Soliton modes for a defocusing medium thus exist in the range of λ , which is complementary to that for a focusing medium. This result basically agrees with the numerical identifications of solitary modes in Fig. 1. In the opposite limit $\lambda \rightarrow -\infty$, for which localized GS modes exist with $\sigma < 0$, the same expressions (26) and (27) formally apply and $N_s(\lambda)$ is found to diverge as $(4\delta^3/9\Omega_0^2\gamma)|\lambda|^2/|\beta|$ in the 2D case and as $|\lambda|^{D/2+1}/|\beta|$ in general. It is worth noticing that in this region ground-state test functions ϕ_0 become poor candidates for approaching $N_s(\lambda)$. In contrast, Gaussians $\sim A e^{-\gamma r^2}$ fit better the domain of large-amplitude ground states. Approximating the nonlinear term efficient at small r with $\sigma|\phi|^2 \approx \sigma A^2(1-2\gamma r^2)$ in Eq. (3), it is readily found that the only positive exponent γ reads for large $A > \sqrt{\Omega_0/|\sigma|}$ as $\gamma \approx \Omega_0^2/8|\sigma|A^2$, which corresponds to negative $\lambda \sim -|\sigma|A^2 \ll -\Omega_0$. So, λ decreases to larger negative values as the soliton amplitude increases in the case $\sigma < 0$. Ignoring the diffraction term in this limit, ϕ may also be given by $\phi \approx [(\lambda+U)/\sigma]^{1/2}$, referred to as the Thomas-Fermi approximation in the 1D case [23]. Here, we get $N_s \approx 2^{2D}\pi|\lambda|^{D/2+1}/[|\sigma|D(D+2)\Omega_0^D]$ at dimensions $D \geq 2$, which is close to the Gaussian limits plotted in Fig. 1 for $\lambda \rightarrow -\infty$. Similar properties characterize 1D ground states of the Gross-Pitaevskii equation, for which higher-order modes were investigated by means of Hermite-Gauss polynomials in Ref. [23].

IV. STEP POTENTIAL

We now apply the above procedure to other potentials capable of stabilizing the collapse of wave functions with integral N below critical. Because the coming examples mainly apply to the field of nonlinear optics where the role of time t is played by the propagation distance z , we will select the space dimension number $D=2$. To start with, we study the action of a step-potential on NLS ground states. This can be viewed as a smoothed version of the circular step potential well for light-guiding media as, e.g., optical fibers that trap the beam energy within a core of finite dimension. Following [10], we consider a medium with a step potential in square form,

$$U(\vec{r}) = -\epsilon H(R-r), \quad (31)$$

where $\epsilon > 0$ and R are the amplitude and core radius of the trap. For soliton widths much less than the core radius R , the potential U reduces to the quadratic form $\sim \epsilon(r^2/R^2 - 1)$ through simple series expansion. The analogy with the previously studied parabolic profile is thus obvious for narrow wave packets. In this approximation, the domain of λ for Eq. (3) with potential (31) is shifted to the right compared with the case of a parabolic potential, as $\lambda_{\text{step}} \approx \lambda_{\text{parabolic}} + \epsilon$. When this limit is not satisfied, i.e., for a beam with typical waist of the order of R , the square form in Eq. (31) must fully be employed. Inserting this into the functional (13) thus yields

$$S_a = \alpha A^2 a^{D-2} - \beta A^4 a^D - \epsilon A^2 a^D \gamma(a) + \lambda \delta A^2 a^D, \quad (32)$$

where, for axis-symmetric beams,

$$\gamma(a) = 2^{D-1} \pi \int_0^{R/a} \xi^{D-1} |\phi_a(\xi)|^2 d\xi. \quad (33)$$

The variational equations (15) are straightforward to establish,

$$-\epsilon \gamma(a) a^2 - (2\beta A^2 - \lambda \delta) a^2 + \alpha = 0, \quad (34)$$

$$-\epsilon a^2 [D + a \partial_a] \gamma(a) - D(\beta A^2 - \lambda \delta) a^2 + (D-2)\alpha = 0, \quad (35)$$

where $\partial_a \gamma(a) = -2^{D-1} \pi R^D a^{-D-1} |\phi_a(R/a)|^2$. An elementary combination provides the relations linking the soliton size a and amplitude A to the soliton parameter λ , namely,

$$2\alpha a^{D-2} = DA^2 a^D \beta + 2^{D-1} \pi \epsilon R^D |\phi_a(R/a)|^2. \quad (36)$$

For $D=2$, the expression for the soliton power follows:

$$N_s(\lambda) = \frac{\delta}{\beta} [\alpha - \epsilon \pi R^2 |\phi_a(R/a)|^2], \quad (37)$$

which can be compared with its equivalent form for a parabolic potential: $N_s(\lambda) = (\delta/\beta) [\alpha - \Omega_0^2 \gamma a^4/4]$ [see Eq. (26)]. In both expressions, the dependence on $a(\lambda)$ induced by the potential modifies the variation of N_s versus λ compared with the free NLS equation ($\epsilon=0$). Imposing now the Gaussian shape, $\phi_a(x) = e^{-x^2/2}$, we obtain

$$N_s(\lambda) = \frac{4\pi}{\sigma} [1 - \epsilon R^2 e^{-R^2/a^2}], \quad (38)$$

where $a^2(\lambda)$ is chosen among the roots of

$$e^{-R^2/a^2} \left[2 \frac{R^2}{a^2} + 1 \right] = 1 - \frac{\lambda \delta}{\pi \epsilon} + \frac{\alpha}{\pi \epsilon a^2}. \quad (39)$$

For $\sigma > 0$, the positiveness of $N_s(\lambda)$ requires the constraint $a^2(\lambda) < R^2/\ln(\epsilon R^2)$ and, therefore, some bound in the range of λ for which GS modes exist. With Gaussian test functions the cutoff λ^* is defined for $e^{-R^2/a^2} = 1/\epsilon R^2$, and it takes the value $\lambda^* = \epsilon - R^{-2} [1 + \ln(\epsilon R^2)]$. From Eqs. (38) and (39), we find that the ratio R/a increases from $R/a \geq 1$ with the parameter λ . Whenever $R/a \gg 1$, $N_s(\lambda)$ tends to its untrapped counterpart ($\epsilon=0$). In other words, when the radius of a square potential becomes very large in front of the soliton width, there is no efficient effect stabilizing the collapse. For this range, $a^2 \approx \alpha/(\delta\lambda - \pi\epsilon)$ makes the soliton exist for $\lambda > \pi\epsilon/\delta$ only and it behaves as the free NLS square width in the limit $\lambda \rightarrow +\infty$. For $\sigma < 0$, N_s exists within the opposite region $0 \leq \lambda \leq \lambda^*$ and $R/a < 1$. In this domain, Eq. (39) indicates that λ cannot access the domain of large, negative values. With $R/a \rightarrow 0$, the solutions become infinitely broad, which limits the existence of localized ground states.

Figure 2(a) shows the variations of $N_s(\lambda)$, which result from numerical integrations of Eq. (3) with the square poten-

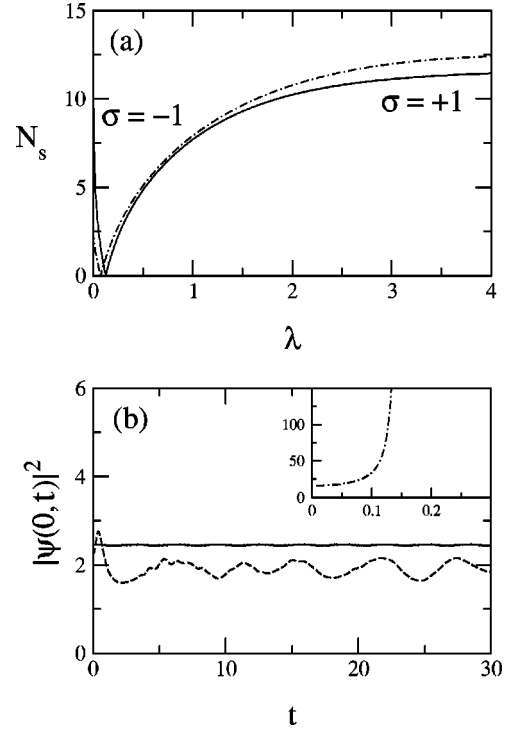


FIG. 2. (a) $N_s(\lambda)$ vs λ for a square potential with $D=2$, $\epsilon=1$, and $R=1.25$ determined from numerical integrations of Eq. (3) (solid curves) and from the variational model with Gaussian test functions (dashed curves). Note that for a defocusing medium GS modes exist within a restricted range of λ , valued around 0. (b) $|\psi(r=0,t)|^2$ versus time for $\sigma=+1$ and Gaussian initial conditions $\psi(r,0) = 1.5 \times e^{-r^2/2}$ with $N \neq N_s < N_c$ (dashed curve) and $\psi(r,0) = 4 \times e^{-r^2/2}$ with $N > N_c$ (dash-dotted curve in the inset). The solid curve refers to the initial condition $N=N_s$ for $\lambda=1$.

tial (31) for $D=2$, $\epsilon=1$, $\sigma=\pm 1$, and $R=1.25$ (solid curves). This is compared with N_s versus λ resulting for the same parameters from a parametric numerical integration of Eqs. (38) and (39). The agreement can be seen to be actually good, apart from the discrepancy $N_c^{\text{Gauss}} = 4\pi > N_c = 11.7$ at large λ . Typically, for $\sigma=+1$, the curve $\lambda=f(R/a)$ increases with the ratio R/a from the value $\lambda^*=0.07$ and the stability region determined by $dN_s/d\lambda > 0$ is limited to $\lambda < 3$, corresponding to $R/a < 2$, while $d_\lambda N_s \rightarrow 0$ for higher λ 's. Direct numerical integration of Eq. (1) with initial conditions close to such soliton modes shows that $\psi(r,t)$ relaxes to a robust shape and undergoes no collapse in that case. Figure 2(b) represents the numerically computed amplitude of ψ at $r=0$, starting from Gaussians with input powers below and above critical, which do not belong to the curve for ground states. We observe that the resulting solution oscillates (dashed curve) or collapses at a finite distance (dash-dotted curve), whenever the power in the initial condition is subcritical or supercritical, respectively. However, the solution integrated from a GS mode at, e.g., $\lambda=1$ (solid curve) preserves its shape. Similarly to anterior results for a parabolic trap [24], small perturbations around the ground state do not increase in time, which confers orbital stability ($d_\lambda N_s > 0$) to such soliton modes.

V. HOLLOW CAPILLARY WAVEGUIDES

We focus our attention on hollow capillary waveguides, for which stabilization of collapse does not directly proceed from the external action of a space-dependent potential, but rather originates from the limitation of the wave diffraction by proper boundary conditions. For this purpose, let us first recall that theoretical investigations of light beams propagating in hollow fibers are currently based on coupled-mode theory [15]. The derivation of the coupled-mode equations starts with the vector-wave equation

$$\vec{\nabla} \times \vec{\nabla} \times \vec{E} - \frac{1}{c^2} \partial_t^2 \int_{-\infty}^t dt' n^2(r, t-t') \vec{E}(t') = \frac{2n_2}{c^2} \partial_t^2 |\vec{E}|^2 \vec{E}, \quad (40)$$

where n and n_2 are the linear and nonlinear components in the refractive index, respectively. In the absence of Kerr nonlinearity, the solution of Eq. (40) consists of a linear superposition of eigenmodes, decomposed into a discrete set of leaky modes and a modal field. As leaky modes are expected to determine the field in and close to the bore, the electric field \vec{E} is usually represented in terms of discrete leaky modes as $\vec{E}(r, \phi, z, t) = (1/2) \sum_{jp} \vec{V}_{jp}(r, \phi) A_{jp}(z, t) e^{ik_{jp}(0)z - i\omega_0 t} + \text{c.c.}$, where the integers j and p are the mode indices, \vec{V}_{jp} refers to the transverse mode profile and A_{jp} denotes the longitudinal complex envelope with central wave number $k_{jp}(0) \approx 2\pi/\lambda_0$ and frequency ω_0 . For a capillary of radius R such as $\lambda_0/R \ll 1$, the leaky-mode solutions of a hollow fiber can be approximately described by a complete set of transverse linearly polarized modes [16]. In this basis, a group of modes indexed by p is preferably excited. In cylindrical geometry, those are defined by $\vec{V}_{jp}(r, \phi) = \hat{x} J_j(u_{jp}r/R) [\sin(j\phi), \cos(j\phi)]$ for $r \leq R$ and $\vec{V}_{jp} \approx \vec{0}$ for $r > R$, where \hat{x} denotes the unit vector in the x direction, and $J_j = J_{j=0,1,2,\dots}$ is the Bessel function of order j , with $u_{jp} = 1, 2, \dots$ being the p th root of the equation $J_j(u_{jp}) = 0$. The mode J_0 is referred to as the fundamental (EH_{11}) mode with $u_{11} = 2.405$. For solid-core fibers, the electric field of the p mode is multiplied by the factor $\sim e^{-L/L_{dp}}$ after a propagation distance L and damping of the laser intensity is minimized for input beams shaped on the fundamental mode $J_0(2.405r/R)$. In recent experiments [17], Gaussian input beams focused on the entrance plane of a tube were observed to convey up to 98% of the incident energy through the capillary over several tens of Rayleigh lengths, when the input beam $E(r) \sim e^{-r^2/w_0^2}$, having $w_0/R \approx 0.6435$, optimized the coupling with the fundamental mode. In these observations, the nonlinearity, however, played a minor role, as the Kerr effect was of little influence in the low-pressure gases filling in the tube. Also, the above theory assumed a first-order expansion of the nonlinear terms in the higher modes, which enters a set of coupled equations governing each mode, viewed as scalar. A first estimate emphasized a power for self-focusing in capillaries exceeding $3 \times N_c$ [15].

When the Kerr effect becomes a key player at high enough input powers, it is, however, necessary to keep all wave components in the Kerr response. For a scalar field, a

basic model thus consists of the free NLS equation (1) with $U=0$, restrained to the bounded domain $0 \leq r \leq R$, i.e., ψ satisfies $\psi(r \geq R, t) = 0$, where the time variable has the meaning of a propagation variable. In this prescription, the decomposition of the electric field in discrete, quasilinear modes is abandoned and the beam is expected to behave as a coherent, fully nonlinear monomode. From this model, it has numerically been shown that 2D beams in a capillary collapse when their power is above the minimum threshold for self-focusing with no trap: $N_c = 11.7$ [18]. It was moreover observed that, for initial data with N below critical, the solution ψ oscillates, instead of dispersing, as the wave does not diffract freely due to the boundedness of the capillary that produces a mode confinement. As N approaches N_c from below, the period in the oscillations becomes larger and larger. This dynamics thus resembles that induced by a parabolic trap. Therefore, we suspect the possibility of forming stable steady-state GS modes in capillaries, whose characteristics are detailed below.

By applying our variational method, the functional \mathcal{S}_a reads as that for the free NLS equation [54]:

$$\mathcal{S}_a = A^2 a^{D-2} \alpha_a - A^4 a^D \beta_a + \lambda A^2 a^D \delta_a, \quad (41)$$

where the integral coefficients α_a , β_a , and δ_a , previously defined by Eq. (14), are now taken over the rescaled variable $\xi = r/a$ with r lying in the bounded domain $0 \leq r \leq R$. These integrals thus depend explicitly on the ratio R/a . In the present scope, let us henceforth focus our attention on the case $D=2$. For a Gaussian test function, $\phi_a = A e^{-r^2/2a^2}$, the integral coefficients in Eq. (41) express as $\alpha_a = \pi [1 - e^{-R^2/a^2} (1 + R^2/a^2)]$, $\beta_a = (\sigma \pi/4) (1 - e^{-2R^2/a^2})$, and $\delta_a = \pi (1 - e^{-R^2/a^2})$. However, unbounded Gaussians alone may be poor candidates for modeling the ground states of the bounded NLS equation, since they cannot satisfy $\phi(r=R) \approx 0$ for broad condensates characterized by moderate ratios R/a . To overcome this problem, we first examine the simple ansatz $\phi(r) = A(\lambda) (1 - r^2/R^2)$ with constant radius in the bounded spatial domain $0 \leq r \leq R$. Elementary calculations then yield $\mathcal{S} = \pi A^2 (2 + \lambda R^2/3) - \sigma \pi A^4 R^2/10$, from which we easily deduce

$$N_s(\lambda) = \frac{5\pi}{3\sigma} (2 + \lambda R^2/3). \quad (42)$$

Equation (42) shows that $N_s(\lambda)$ increases linearly with λ from the cutoff value $\lambda^* = -6/R^2$. For a defocusing medium ($\sigma < 0$), N_s increases to large values as λ covers the range $[-6/R^2, -\infty[$. For a focusing medium ($\sigma > 0$), N_s also increases with λ to N_c , below which collapse cannot occur. This limits the range of validity of (42) to $\lambda^* \leq \lambda < 0.7/R^2$.

Keeping these observations in mind, we propose the ansatz $\phi(r) = A e^{-r^2/2a^2} (1 - r^2/R^2)$, that insures $\phi(r=R) = 0$. Logically, this trial function should correctly describe the range of low λ 's at small ratios R/a , for which the Gaussian reduces to the unity as above, and that of large positive λ 's at

high R/a , for which Gaussians can model narrow GS. For this test function, simple calculations lead to the action integral

$$\begin{aligned} S_a = & \frac{\pi A^2}{R^4/a^4} F_1(R/a) - \sigma \frac{\pi A^4 R^2}{R^{10}/a^{10}} F_2(R/a) \\ & + 2\pi\lambda \frac{A^2 a^2}{R^4/a^4} F_3(R/a), \end{aligned} \quad (43)$$

where $F_1(x) = 2 + x^4 - 2(1 + x^2)e^{-x^2}$, $F_2(x) = 3(1 - e^{-2x^2}) - 6x^2 + 6x^4 - 4x^6 + 2x^8$, and $F_3(x) = 1 - e^{-x^2} - x^2 + x^4/2$. The variational equations for A and a then follow as

$$\frac{R^4}{a^4} F_1(R/a) - \sigma \frac{A^2 a^2}{4} F_2(R/a) + 2\lambda a^2 \frac{R^4}{a^4} F_3(R/a) = 0, \quad (44)$$

$$\begin{aligned} 4 \frac{R^4}{a^4} \left[F_1(R/a) - \frac{R^4}{a^4} (1 + e^{-R^2/a^2}) \right] - \sigma \frac{A^2 a^2}{2} F_4(R/a) \\ + 2\lambda a^2 \frac{R^4}{a^4} F_5(R/a) = 0, \end{aligned} \quad (45)$$

with $F_4(x) = (15/2)(1 - e^{-2x^2}) - 3x^2(4 + e^{-2x^2}) + 9x^4 - 4x^6 + x^8$ and $F_5(x) = 6 - 4x^2 + x^4 - 2(3 + x^2)e^{-x^2}$. From these relations, we then obtain the variation of N_s versus λ ,

$$N_s(\lambda) = \frac{8\pi}{\sigma} F_3(R/a) \frac{F_1(R/a) + 2\lambda a^2 F_3(R/a)}{F_2(R/a)}. \quad (46)$$

For $R/a < 1$, Eq. (46) tends to the limit (42), i.e., for large radius a , the soliton is close to that modeled by the function $A(1 - r^2/R^2)$. Its localization only proceeds from the walls of the capillary. In the opposite limit, $R/a > 1$, one has $N_s \simeq (2\pi/\sigma)(1 + \lambda a^2)$, where $\lambda a^2 \rightarrow 1 - 8a^4/R^4$, and N_s increases to the self-focusing threshold for Gaussians, as expected. At small amplitudes, $A^2 \rightarrow 0$, the cutoff parameter λ^* separating the existence domains for soliton modes in focusing and defocusing media is given by

$$\lambda^* \simeq - \frac{(R/a)^2 F_1(R/a)}{2R^2 F_3(R/a)}. \quad (47)$$

Computing λ^* in the limit of small ratios R/a restores $\lambda^* \simeq -6/R^2$. Pushing R/a to 1 we moreover find $\lambda^* \simeq -5.79/R^2$. For $\sigma > 0$, the variations of R/a versus λ indeed show a monotonous increase of λ , close to $\lambda \simeq 5R/a - 8$, as the ratio R/a is augmented from $R/a = 1$. So, the range of low λ concerns moderate values of R/a . For $\sigma < 0$, GS modes with positive N_s exist whenever $R/a < 1$, which corresponds to the domain in λ decreasing from λ^* to larger negative values.

To cure the discrepancy between the Gaussian threshold $N_c = 4\pi/\sigma$ and the exact threshold for self-focusing $N_c = 11.7/\sigma$ in the range of large, positive $\lambda > 0$ ($R/a \gg 1$, $\sigma = +1$), we model the ground state for a capillary with the free NLS ground state, ϕ_0 , which satisfies the equation $-\phi_0 + \nabla^2 \phi_0 + \phi_0^3 = 0$. Since we look for solutions ϕ with

size less than the capillary radius, it is natural to consider the action functional $\mathcal{S} = \int \{ |\nabla \phi|^2 - (\sigma/2)|\phi|^4 + \lambda|\phi|^2 \} d\vec{r}$, whose integrals are taken over the whole spatial domain, and subtract the same integrals taken for $R < r < +\infty$. In this range, the NLS ground state asymptotically tends to the function

$$\phi_0(r) \sim B r^{-1/2} \exp(-r) \quad (48)$$

at large distances ($r \gg 1$), where

$$B = \left(\frac{\pi}{2} \right)^{1/2} \int_0^{+\infty} \phi_0^3(r') I_0(r') r' dr' \simeq 3.52,$$

and I_0 is the zeroth-order modified Bessel function. Since $\phi_0(r)$ does not satisfy $\phi_0(r=R) = 0$ at finite $R > 1$, it is moreover requested to weight it with, e.g., the step function $H(R-r)$. Thus, we insert the test function $\phi(r) = A(\lambda) \phi_0[r/a(\lambda)] H(R-r)$ into \mathcal{S} . In the gradient norm of the action integral, the integrand expresses as $|\partial_r \phi|^2 = [\partial_r \phi_0 H(R-r) - \delta(R-r) \phi_0]^2$, where the second term mainly contributes to this integral at $r=R$ only, with $\phi_0(r=R)$ close to zero ($\phi_0/\partial_r \phi_0|_{r=R} \ll 1$). Approximating $|\partial_r \phi|^2 \simeq (\partial_r \phi_0)^2 H(R-r) - \delta(R-r) H(R-r) \partial_r \phi_0^2$, we derive \mathcal{S}_a in the form

$$\begin{aligned} \mathcal{S}_a = A^2 \left\{ N_c + \pi B^2 \left[3 \left(1 + \frac{a}{2R} \right) \exp(-2R/a) - \Gamma[0, 2R/a] \right] \right\} \\ - \sigma A^4 a^2 \{ N_c - \pi B^4 \Gamma[0, 4R/a] \} \\ + \lambda A^2 a^2 \{ N_c - \pi B^2 \exp(-2R/a) \}, \end{aligned} \quad (49)$$

where $\Gamma[0, x]$ is the standard gamma function. Performing the functional variations of \mathcal{S}_a with respect to A and a then leads to

$$\begin{aligned} N_c + \pi B^2 \left\{ 3 \left(1 + \frac{a}{2R} \right) \exp(-2R/a) - \Gamma[0, 2R/a] \right\} \\ - 2\sigma A^2 a^2 (N_c - \pi B^4 \Gamma[0, 4R/a]) \\ + \lambda a^2 [N_c - \pi B^2 \exp(-2R/a)] = 0, \end{aligned} \quad (50)$$

$$\begin{aligned} 2\pi B^2 \left(1 + \frac{3R}{a} + \frac{3a}{4R} \right) \exp(-2R/a) - \sigma A^2 a^2 (2N_c \\ - \pi B^4 \{ \exp(-4R/a) + 2\Gamma[0, 4R/a] \}) \\ + 2\lambda a^2 [N_c - \pi B^2 (1 + R/a) \exp(-2R/a)] = 0. \end{aligned} \quad (51)$$

Therefore,

$$\begin{aligned} N_s(\lambda) = \frac{[N_c - \pi B^2 \exp(-2R/a)]}{2\sigma(N_c - \pi B^4 \Gamma[0, 4R/a])} (N_c + \pi B^2 \{ 3(1 \\ + a/2R) \exp(-2R/a) - \Gamma[0, 2R/a] \}) \\ + \lambda a^2 [N_c - \pi B^2 \exp(-2R/a)]. \end{aligned} \quad (52)$$

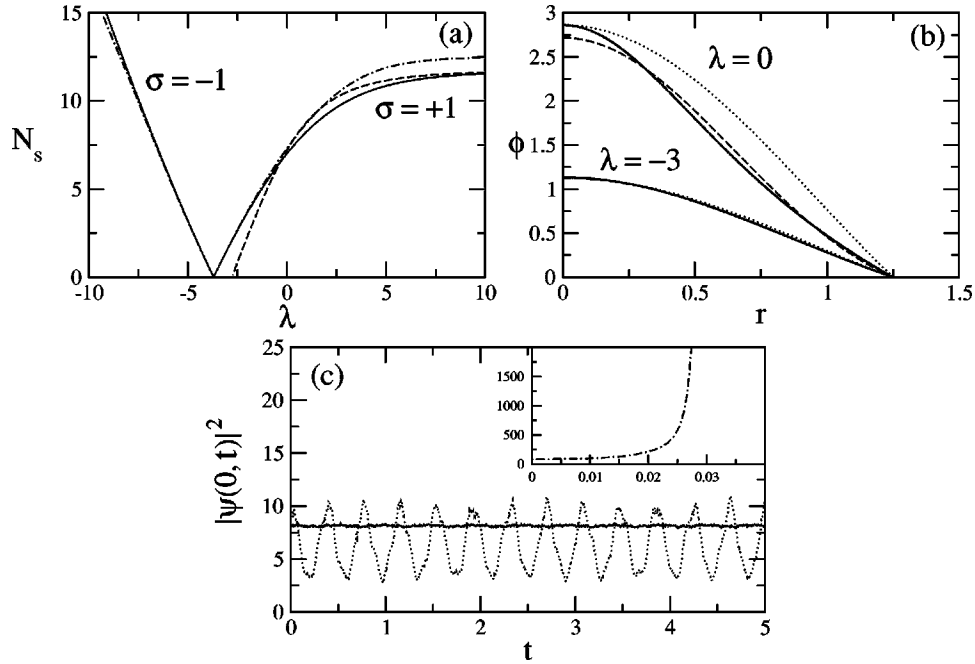


FIG. 3. (a) N_s vs λ for a hollow capillary waveguide with $R=1.25$. Numerical integration of Eq. (3) with $U=0$ is represented by the solid curve; the dash-dotted and dashed curves represent the variational approximations using truncated Gaussians and free NLS GS, respectively. The parametric regions in λ for which $d_\lambda N_s > 0$ are restricted to $\lambda < 3$, which leads to $R/a_{\min} \approx 2.2$. (b) Numerically identified GS modes for different $\lambda \geq \lambda^* = -5.78/R^2$ are plotted by solid lines for $R=1.25$ ($\lambda = -3$, lower profile, $\lambda = 0$, upper profile). They lie close to the Bessel function $AJ_0(2.405r/R)$ (dotted curves) at weak amplitudes only ($\lambda = -3, A \approx 1.12$) and depart from it at higher amplitudes ($\lambda = 0, A \approx 2.8$). For comparison, truncated Gaussian trial functions are plotted by the dashed line for the same λ 's. (c) $|\psi(r=0,t)|^2$ versus time for $\sigma = +1$ and initial conditions using truncated Gaussians $\phi(r) = Ae^{-r^2/2a^2}(1-r^2/R^2)$ with $N = 5.17 \neq N_s < N_c$ ($A = 3, a = 0.5$, dotted curve), and with $N = 4N_c$ ($A = 9.028, a = 0.5$, dash-dotted curve in the top inset). The solid curve refers to the initial condition $N = N_s$ for $\lambda = 0$.

Similarly to the previous Gaussian modeling, λ monotonically increases from -2.5 to infinity as R/a grows from the value $R/a = 1.41$. At large R/a , it is found that the soliton size behaves like $a^{-1}(\lambda) \approx \sqrt{\lambda}$, as expected.

We have superimposed the results obtained from the Gaussian modeling and its asymptotic correction using ϕ_0 in Fig. 3(a) for the bore radius $R=1.25$. The analytical result again exhibits a good agreement with the numerics that solves Eq. (3) with $U=0$ and $\phi(r \geq R) = 0$. The cutoff parameter revealed numerically, $\lambda^* \approx -5.78/R^2$, perfectly agrees with that evaluated from truncated Gaussians. For $\sigma = +1$, the power in a stable self-guided mode must be below the critical self-focusing threshold, and numerical calculations show that $d_\lambda N_s > 0$ is fully satisfied for $\lambda^* < \lambda < 3$. At relatively weak nonlinearities ($\lambda < 0$), the ground state is close to the linear fundamental mode $J_0(2.405r/R)$. The slope $d_\lambda N_s$ is maximum, which may justify why the Bessel mode is capable of promoting a quasiperfect monomode guiding over spectacular distances in hollow capillaries. Comparatively, the variational approach emphasizes that $\lambda_{\max} = 3$ bounds from above the range of stability of GS modes, which yields $R/a_{\min} = 2.2$. This value restores the ratio $\sqrt{2}a/R = w_0/R = 0.6435$, which was claimed to optimize the coupling of optical Gaussian beams with the fundamental mode. At moderate N_s , the Bessel mode ensuring the best entrance coupling with the capillary is attained, which is il-

lustrated by Fig. 3(b). In that case, the variational trial function employing the truncated Gaussian ansatz almost completely superimposes with the fundamental mode at low λ near the cutoff λ^* . For higher N_s ($\lambda \geq 0$), the solution ϕ , still corresponding to stable waveguides, departs from the Bessel mode to reach the ground state of the unbounded NLS equation ($U=0$).

Figure 3(c) shows the amplitude of ψ centered at $r=0$ resulting from a direct numerical integration of Eq. (1) with Gaussians having input powers below and above critical, which do not belong to the curve plotted in Fig. 3(a). As expected, we observe that the resulting solution either oscillates (dotted curve) or collapses at a finite distance (dash-dotted curve). Note that, owing to the boundary conditions, radiation trapped in the waveguide bounces back and forth, which introduces a perturbative noise affecting the evolution of the peak intensity. In spite of this, the solution initially lined up on a ground state ($\lambda = 0$) keeps a robust shape (solid curve).

VI. VORTEX STATES AND FLOWING OBSTACLES

A. Pure vortex states

In focusing media with saturable nonlinearity, single vortex states are stable for $U=0$ against radial perturbations whenever $d_\lambda N_s > 0$, and unstable against azimuthal perturba-

tions that break the cylindrical symmetry [31]. Azimuthal perturbations are furthermore able to split higher-order vortices into $2|m|$ daughter GS solitons in the same media [32]. With no saturation, it will thus be interesting to see if VS modes satisfying the stability criterion $d_\lambda N_s > 0$, valid for radial perturbations, will still hold their shape in a parabolic trap, or if collapse will affect their ring structure at high enough powers. In the absence of trap, vortex modes with $m = 1$ were indeed observed to be unstable, i.e., to diffract or collapse, when the power in the initial condition for Eq. (1) was below or above that of the mode, respectively [59]. In defocusing media like BECs with repulsive interactions, there is no collapse dynamics. 2D vortices with $|m|=1$ are expected to be stable, whereas multi-charged ones are generally unstable and break up into m vortices with unit charge [40,41]. In what follows, we comment on the changes in the radial stability properties between vortices and GS modes for a parabolic potential $U(r) = \Omega_0^2 r^2/4$. For $D=2$, we consider the functional

$$\begin{aligned} \frac{\mathcal{S}}{2\pi} = & \int_0^{+\infty} |\partial_r \chi|^2 r dr + m^2 \int_0^{+\infty} \frac{|\chi|^2}{r} dr - \frac{\sigma}{2} \int_0^{+\infty} |\chi|^4 r dr \\ & + \frac{\Omega_0^2}{4} \int_0^{+\infty} r^3 |\chi|^2 dr + \lambda \int_0^{+\infty} |\chi|^2 r dr. \end{aligned} \quad (53)$$

From the asymptotic arguments displayed in Sec. II we employ the ring-shaped test function $\chi = A_m \chi_{a,m}(r/a_m)$ with $\chi_{a,m}(\xi = r/a_m)$ defined by Eq. (17). Such solutions have the power integral for the m th mode,

$$N_m = 2\pi a_m^2 A_m^2 \int_0^{+\infty} \frac{\xi^{2|m|+1} e^{-\xi^2}}{(B_m + \xi)^{2|m|}} \xi d\xi. \quad (54)$$

Inserting this test function into Eq. (53) yields the transformed functional

$$\begin{aligned} \mathcal{S}_a = & A_m^2 \alpha_m(B_m) - a_m^2 A_m^4 \beta_m(B_m) + \frac{\Omega_0^2}{4} a_m^4 A_m^2 \gamma_m(B_m) \\ & + a_m^2 A_m^2 \lambda \delta_m(B_m), \end{aligned} \quad (55)$$

with integral coefficients

$$\begin{aligned} \alpha_m(B_m) = & 2\pi \int_0^{+\infty} \frac{\xi^{2|m|+1} e^{-\xi^2}}{(B_m + \xi)^{2|m|}} \left[\frac{B_m^2 m^2}{\xi^2 (B_m + \xi)^2} - \frac{2B_m |m|}{(B_m + \xi)} \right. \\ & \left. + \xi^2 + \frac{m^2}{\xi^2} \right] d\xi, \end{aligned} \quad (56)$$

$$\beta_m(B_m) = \pi \sigma \int_0^{+\infty} \frac{\xi^{4|m|+1} e^{-2\xi^2}}{(B_m + \xi)^{4|m|}} d\xi, \quad (57)$$

$$\gamma_m(B_m) = 2\pi \int_0^{+\infty} \frac{\xi^{2|m|+3} e^{-\xi^2}}{(B_m + \xi)^{2|m|}} d\xi, \quad (58)$$

$$\delta_m(B_m) = 2\pi \int_0^{+\infty} \frac{\xi^{2|m|+1} e^{-\xi^2}}{(B_m + \xi)^{2|m|}} d\xi. \quad (59)$$

Here, the Lagrange parameters A_m , B_m , and a_m are all positive and the integral coefficients depend on B_m explicitly. \mathcal{S}_a for Gaussian-approximated GS solitons is refound when setting $m = B_m = 0$. The configuration $m = 0$ with $B_0 \neq 0$ corresponds to the radially symmetric ring-shaped mode already studied in Ref. [22], which we do not consider here. Derivatives of Eq. (55) with respect to A_m and a_m formally lead to the same equations as Eqs. (26) and (27),

$$A_m^2(\lambda) = \frac{1}{2\beta_m} [2\lambda \delta_m + \Omega_0^2 a_m^2 \gamma_m], \quad (60)$$

$$a_m^2(\lambda) = \frac{\sqrt{\lambda^2 \delta_m^2 + 3\alpha_m \gamma_m \Omega_0^2} - \lambda \delta_m}{\frac{3}{2} \Omega_0^2 \gamma_m}. \quad (61)$$

The third variational equation, $\delta \mathcal{S}_a / \delta B_m = 0$, yields in principle the explicit dependence of the vortex parameters over the couple (λ, m) . Among the coefficients (56)–(59), with $|m| \geq 1$ and $B_m > 0$, the integrands with higher exponent lead to smaller integrals than their counterparts for $m = B_m = 0$. Therefore, the value of $\beta_{m \neq 0}$ is smaller than that for the GS modes, and much smaller than the new values of δ_m and γ_m . Thus, for a focusing medium ($\sigma > 0$), $A_m^2(\lambda)$ increases in absolute value. In addition, assuming that the integral α_m is mainly given by the contributions at small $\xi \ll 1$ in the integrand, we deduce that the ratio α_m / γ_m should be larger than $\alpha / \gamma = 1$ for $m = B_m = 0$, while δ_m / γ_m will remain nearby the unity. On the whole, the curve $N_s(\lambda, m) = \delta_m(B_m) A_m^2 a_m^2$ for vortices should lie *above* its counterpart for GS modes whenever $\sigma > 0$. Moreover, as the changes in γ_m and δ_m are similar, the cutoff value $\lambda^* = -\Omega_0 \sqrt{\alpha_m \gamma_m} / \delta_m$ should lie at a smaller (more negative) value, i.e., $\lambda_{\text{vortex}}^* < \lambda_{\text{GS}}^*$. For a defocusing medium ($\sigma < 0$), since $N_s(\lambda, m) \rightarrow (4\delta_m^3 / 9\Omega_0^2 \gamma_m) |\lambda|^2 / |\beta_m|$ with $\delta_m \leq \delta_{m=0}$ at large negative λ , the vortex mass $N_s(\lambda, m)$ should finally remain below that for a GS mode.

Because the coefficients (56)–(59) depend on cumbersome transcendental functions, we determine an appropriate parameter B_m by using relations (8) and (9) in the combined form

$$\int_0^{+\infty} \{\lambda |\chi|^2 - |\partial_r \chi|^2 - (m^2/r^2) |\chi|^2 + (3\Omega_0^2/4)r^2 |\chi|^2\} r dr = 0. \quad (62)$$

After inserting the vortex ansatz, we minimize numerically this relation by searching for the value of B_m at, e.g., $|m| = 1$, which makes the smallest left-hand side (LHS) in expression (62) for given $a \sim 1/\sqrt{\lambda} = 1$. Under such conditions, this LHS decreases to zero for increasing integer values of B_m , but it stays real-valued for $B_m = 1$ only. This makes the LHS of Eq. (62) much smaller than unity. For this value of B_m , we get $\alpha_1(1) \approx 1.824$, $\beta_1(1) \approx 0.0227$, $\gamma_1(1) = 0.984$, and $\delta_1(1) = 0.66$. For higher B_m 's these coefficients decrease

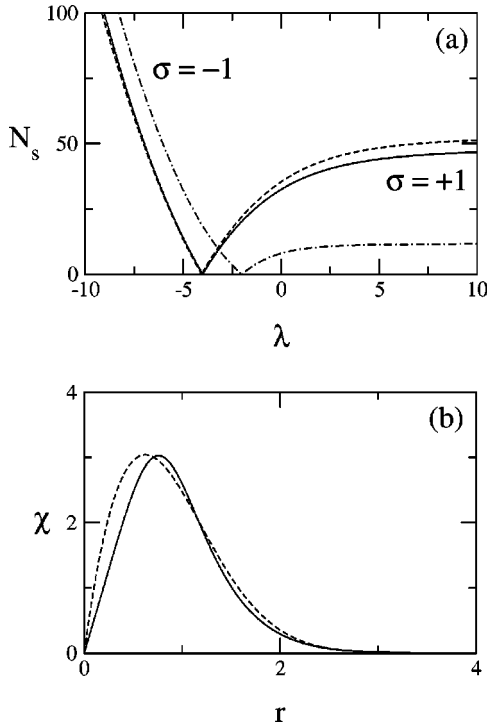


FIG. 4. (a) $N_s(\lambda)$ vs λ for vortex states of Eq. (3) with a parabolic trap, $|m|=1$, $D=2$, in both cases $\sigma = +1$ and $\sigma = -1$. Results from numerical integrations of Eq. (3) are represented by the solid curves; variational results are plotted as dashed lines. The dash-dotted curve recalls the same variations for the 2D NLS ground state, computed numerically. (b) Radial profile $\chi(r)$ of a vortex solution with $m = +1$, computed for $\lambda = +1$ from the variational method [dashed curve: $A_1(1) = 9.38739$, $a_1^2(1) = 0.6818$, $B_1(1) = 1$] and from direct numerical integration of Eq. (3) (solid curve).

as, e.g., $\gamma_1(B_m)$, $\delta_1(B_m) \sim \gamma_1(1)/B_m$, $\delta_1(1)/B_m$. Figure 4(a) shows a plot of $N_s(\lambda, m)$ versus λ obtained from numerical integrations of Eq. (3) by standard shooting techniques for $\phi = \chi(r)e^{im\theta}$ satisfying $m = +1$, $\chi(0) = 0$ and $\chi_r(0) = 0$. This figure compares direct numerical results with $N_1(\lambda)$ obtained from Eqs. (60) and (61) when using $B_1 = 1$. Both focusing and defocusing nonlinearities for ring-shaped states at the order $m = +1$ are shown. The agreement between the numerical and analytical results is good, up to the usual discrepancy for $\lambda \gg 1$. It can be noticed that the variation of $N_s(\lambda)$ is quite close to that for the radially symmetric states of Eq. (3) with $m = 0$ numerically revealed in Ref. [22]. At large $\lambda > 10$, for which the solution no longer feels the trap influence, the vortex power exceeds $N_s \approx 47$, which agrees with the numerical evaluation of the critical power for the collapse of vortices, $N_s \approx 48.7$, measured by Kruglov *et al.* in Ref. [60] in the absence of trap. Fig. 4(b) shows the numerically computed (solid line) and the variationally approached (dashed line) radial profile $\chi(r)$ of the vortex with $|m|=1$, corresponding to the soliton parameter $\lambda = +1$ for a focusing medium ($\sigma = +1$).

Illustrating the stability of VS structures with a focusing nonlinearity ($\sigma = +1$), Figure 5 displays 3D plots of vortex intensities at different times, with perturbed initial conditions fitting at leading order a noncollapsing VS mode with N_s

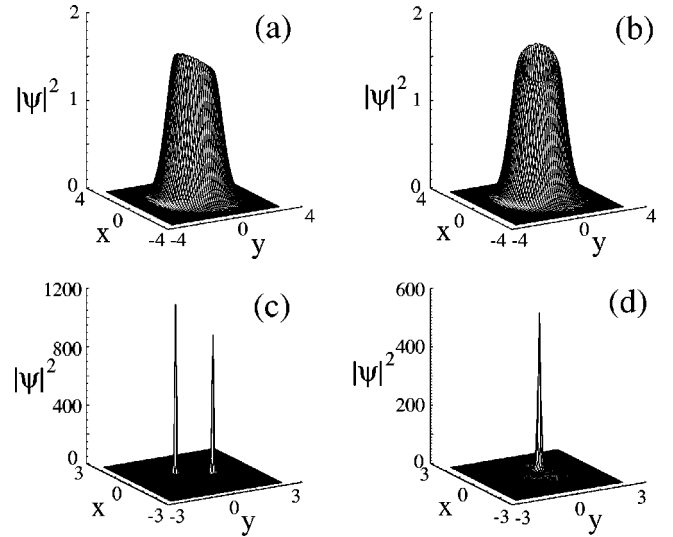


FIG. 5. 3D plots of $|\psi(x,y,t)|^2$ at different snapshots in time for (a) an initial ($t=0$) noncollapsing singly charged VS mode ($\lambda = -3$) with 5% azimuthal perturbation, (b) the same vortex at $t = 20$, (c) the break-up pattern and collapse of a high-power VS mode ($m = 1, \lambda = 4$) at $t = 4$, being perturbed by the local numerical noise only, and (d) one-peaked collapse of the previous mode initially undergoing a 5% azimuthal perturbation, shown at $t = 0.4$.

$< N_c = 11.7$ ($\lambda = -3$) and another one with much higher N_s ($\lambda = 4$). With powers below the usual threshold for collapse, vortex modes cannot blow up. This follows from the key estimate $H \geq (1 - N/N_c) \int |\nabla \psi|^2 d\vec{r}$, according to which collapse producing a blow up in the gradient norm can only occur for powers above critical [55], which still applies to vortices. Figure 5(a) shows a subcritical ($N_s < N_c$) VS mode with 5% azimuthal perturbation at $t = 0$, i.e., $\psi(x,y,0) = \chi(r)e^{im\theta} [1 + 0.05 \cos(q\theta + 0.4)]$ with, for the present case, $m = q = 1$. This initial state does not blow up at later times. Instead, it keeps a robust radial shape and just undergoes a rotation of $\theta = -\pi/2$ at $t = 20$ [Fig. 5(b)]. In contrast, a VS mode having a supercritical power ($N_s > N_c$ at $\lambda = 4$) either decays into $2|m|$ collapsing spikes due to instability only induced by the numerical noise [Fig. 5(c) at $t = 4$], or it rapidly collapses as a whole when it undergoes the former perturbation [Fig. 5(d) at $t = 0.4$]. These results indicate that vortices keep a stable radial shape, as long as the condition for no collapse, $N_s < N_c$, holds. Otherwise, they collapse and the stability criterion $d_\lambda N_s > 0$ is no longer sufficient for insuring stable vortices. The lack of orbital stability of single vortices caused by azimuthal perturbations has been shown in Ref. [31] for saturating nonlinearities. In this respect, we recall that the stability proof basically requires stationary modes having no node in their spatial distribution for assuring the absence of growth in the perturbations (see, e.g., Ref. [24] for GS modes of the GP equation). For vortices having one node, this constraint is not satisfied, and the discrete spectrum of the NLS operators governing the perturbations generally contains unstable modes.

For similar reasons, the stability criterion $d_\lambda N_s > 0$ becomes in principle invalid for multicharged (higher order) vortices with $|m| > 1$. To check this point, we have performed

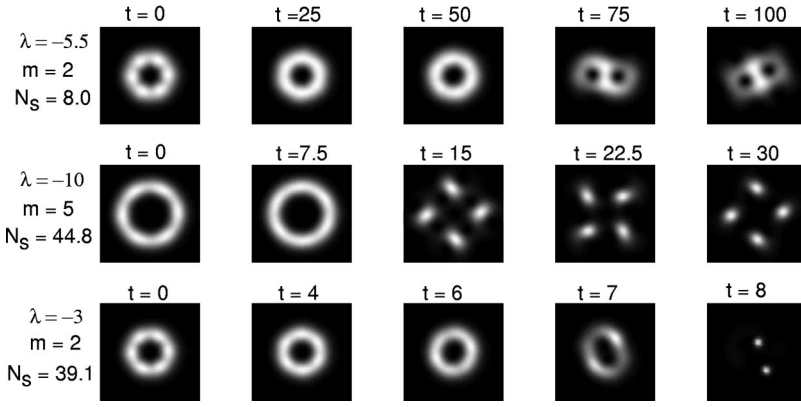


FIG. 6. Instability patterns of multiple charged vortices undergoing 5% azimuthal perturbations: $\psi(x,y,0) = \chi(r)e^{im\theta}[1 + 0.05 \cos(6\theta + 0.4)]$. Top row: decay of a twofold VS mode with $N_s < N_c$ into two singly charged vortices. Middle row: breakup of a fivefold vortex with $N_s > N_c$ into four rotating spikes. Bottom row: splitting of a supercritical twofold vortex into two collapsing spikes.

numerical runs, always concerned with a focusing medium ($\sigma = +1$), in which m -fold quantized vortices with $m > 1$ are initially perturbed by the 5%-amplitude oscillations defined above. As shown in the top row of Fig. 6, a multicharged vortex with $m=2$ and particle number N_s below the critical threshold for collapse decays into two singly charged vortices orbiting around each other under modulations with $q=6$. This property of unstable high-order vortices for attractive interactions corroborates some previous theoretical expectations [41] summarized in Sec. I. Our simulation, however, allows us to specify the instability dynamics. First, when no collapse occurs ($N_s < N_c$), a high-order vortex seems “robust” to some extent, in the sense that high-order modulations of the vortex ring produce a limited number of elementary singly charged vortices that develop rather slowly in time. This was confirmed by numerical runs performed with $m=5$, for which no instability occurred before large times $t < 100$ (not shown here). Second, with $N_s > N_c$, we observe a rich variety of dynamics, whose patterns depend on the initial conditions and all conclude to the instability of high-order vortices. Briefly speaking, a supercritical condensate is capable of either decaying into several “stable” elementary spikes rotating around the trap, each having a particle number below N_c , or of breaking up into collapsing spikes otherwise. The middle and bottom rows of Fig. 6 illustrate the fates of vortices for which the VS mode has an integral N_s either below or above N_c times the number of final spikes. In collapse regimes, the dynamics appears to be strongly sensitive to the number of azimuthal modulations along the vortex ring. With $q=2$ for instance, we observed that the $m=5$ vortex of Fig. 6 was rapidly broken up into two collapsing spikes. In the light of these observations, we summarize VS instability in focusing media with parabolic trap as follows. (i) Vortex stability is limited to particle numbers $N_s < N_c$ for attractive interactions. (ii) When this constraint is satisfied, single vortex states are stable, but multiple charged vortices are unstable and they can decay into $|m|$ single vortices. (iii) When this constraint is not satisfied, high-order vortices split into several elementary spikes that can collapse if their individual number of particles is above critical. Some of these patterns could experimentally be verified in future works on attractive BECs.

B. GS/vortex formation in dilute inhomogeneous BECs

Our formalism may help in approximating the elementary solutions of more complicated issues as, e.g., the GS modes

and localized vortices of a dilute atom condensate trapped in a harmonic well and passing through an object (see, e.g., Ref. [48]). For example, the object can arise from a light-induced Gaussian potential barrier, moving with velocity \bar{v} along one axis, and the BEC wave function obeys the 2D NLS Eq. (1) with $\nabla^2 = \partial_x^2 + \partial_y^2$ and

$$U(x,y) = \frac{\Omega_0^2}{4}(x^2 + y^2) + c \exp[-bx^2 - b(y - \bar{v}t)^2], \quad (63)$$

with $\Omega_0 = 1$ and constants $c, b > 0$. For repulsive condensates, σ is taken as negative ($\sigma = -8\pi\mathcal{N}|a_0|$ where \mathcal{N} is the physical number of atoms in BECs and $|a_0|$ the scattering length). Two kinds of stationary/travelling-wave modes are then interesting to study, namely: (i) The GS solutions that serve as initial data at $t=0$ for an object initially centered at origin $(0,0)$ in the plane (x, y) . (ii) The vortex solutions possessing an orbital angular momentum and azimuthal angle θ . These vortices are created once the object moves along the y axis and produces a local disturbance, which propagates through the BEC fluid at times $t > 0$. Reversely, as recalled in Sec. I, the flow around the object creates a drag force beyond a threshold velocity, which is linked to the emission of vortices generated at opposite sides of the object in order to dissipate and reduce the high local flow speed [50]. In the present scope, we only attempt to model the initial stationary state (i). To determine its shape, we may equivalently employ the previous functional \mathcal{S}_a or directly insert appropriate trial functions into the integral relations (8)–(10). At $t=0$ the object has a zero velocity and the fluid adopts the shape of a GS soliton with speed and momentum both equal to zero. U thus reduces to $U(r) = \Omega_0^2 r^2/4 + ce^{-br^2}$, which preserves the radial symmetry. For solutions in the form $\phi(r) = A\phi_a(r/a)$, the set of Eqs. (8) and (9) provides the amplitude of the soliton, given as

$$A^2(\lambda) = \frac{\lambda\delta}{\beta} + \frac{\Omega_0^2}{2\beta}a^2\gamma + \frac{c}{\beta} \int (1 - ba^2\xi^2)e^{-ba^2\xi^2} |\phi_a(\xi)|^2 d\vec{\xi}, \quad (64)$$

while the soliton radius follows from the roots of

$$\frac{3}{4}\Omega_0^2\gamma a^4 + a^2\delta\lambda - \alpha + a^2c \int (1 - 2ba^2\xi^2)e^{-ba^2\xi^2}|\phi_a(\xi)|^2 d\xi = 0. \quad (65)$$

With a Gaussian modeling, $\phi_a(r/a) = e^{-r^2/2a^2}$, these relations simplify into

$$A^2(\lambda) = \frac{4}{\sigma} \left[\lambda + \frac{\Omega_0^2 a^2}{2} + \frac{c}{(1+a^2b)^2} \right], \quad (66)$$

$$\frac{3}{4}\Omega_0^2 a^4 + a^2\lambda - 1 + \frac{a^2c(1-ba^2)}{(1+ba^2)^2} = 0, \quad (67)$$

and it is seen right away that the initial GS number of particles is

$$N_s(\lambda) = \delta A^2 a^2 = \frac{4\pi}{\sigma} \left[1 - \frac{\Omega_0^2 a^4}{4} + \frac{bca^4}{(1+ba^2)^2} \right]. \quad (68)$$

For repulsive interactions between bosons, $\sigma = -1$, $N_s(\lambda)$ is an increasing function of $-\lambda$ in the range $\lambda < \lambda^* = -\Omega_0$. Here, $a^2(\lambda)$ increases with $-\lambda$, in such a way that a GS mode with given N_s exists for $c \neq 0$ at lower λ than in the case $c = 0$. This property agrees with Ref. [48], where a GS mode was found at $\lambda = -9.003$ for $c = 0$, while the same parameter should be decreased to $\lambda = -9.208$ for $c = 30$ and $b = 3$. The new GS undergoing the trap augmented by the Gaussian barrier ($c \neq 0$) feels a depletion of density in the trap center due to the presence of the obstacle. At fixed $N_s(\lambda)$, this amounts to decreasing λ . A simple parametric plot eliminating a^2 between Eq. (68) and Eq. (67) indeed shows that with $c = 30$, $b = 3$, the same number of particles N_s as the one without object is refound at a slightly lower value of λ approaching -10 from above, which is compatible with the numerical results of Ref. [48].

When the object begins to move, vortex formation is favored and vortices arise in the wake of the object flow. Determining the resulting travelling vortices becomes difficult to treat analytically. In the presence of a Gaussian obstacle, the fluid indeed decomposes into a vortex pair with opposite vorticities. Interaction of vortex pairs should thus require the definition of two separate test functions involving their mutual separation distance as an additional parameter, which is out of the scope of the present analysis.

VII. CONCLUSION

We have elaborated on a variational method capable of approximating the stationary ground-state and vortex modes of the NLS equation with an external, space-dependent potential. This method enabled us to estimate analytically the variations in the power integral or number of particles, $N_s(\lambda)$, contained in an elementary mode with respect to the

frequency parameter λ , and then to figure out the related variations of the soliton size $a(\lambda)$. By doing so, we were, in particular, able to predict the regions in (N_s, λ) for which such modes are stable following the standard criterion $dN_s/d\lambda > 0$ for soliton stability

Basically, the key point consists in constructing a suitable candidate for the test function entering the variational approach. This can be done by matching the behavior of ϕ , solution to Eq. (3), at small r with that at large r . For parabolic inhomogeneities, ground states exhibit a spatial distribution close to Gaussians, namely $\phi(r) = Ae^{-\gamma r^2}$. For $U = \Omega_0^2 r^2/4$, such solutions with $\gamma = \Omega_0/4$ and $\lambda = \lambda^* = -D\Omega_0/2$ exactly solve Eq. (3), whenever $\sigma \rightarrow 0$, i.e., in the cases of weak nonlinearities and/or at large distances. These limits suit the behaviors of N_s vs λ for small powers, nearby the cutoff parameter λ^* separating the focusing case $\sigma > 0$ from the defocusing one $\sigma < 0$. Gaussians furthermore supply a reasonably good approximation of these ground states for large negative λ 's when $\sigma < 0$. They must, however, be abandoned to the benefit of the free NLS ground-states for $\sigma > 0$, in the limit of large positive λ 's, for which $A(\lambda)$ increases while the soliton size decreases and Eq. (3) mainly reduces to the free ($U = 0$) NLS equation. The same observation holds for a step potential. Note that whatever $U > 0$ may be, bounded or not, the potential always helps in forming localized solution ϕ with similar properties. These properties straightforwardly emerge from the integral relations (8), (9), and (10). For instance, in Eq. (9), it is clear that as $|\lambda| \rightarrow +\infty$, the integral term including U and the gradient norm become negligible, so that $\lambda N \sim (\sigma D/2) \int |\phi|^4 d\vec{r}$. Thus, the domain of large soliton parameters λ rather concerns high-amplitude ground states for which nonlinearities are dominant. Conversely, for weak nonlinearities ($|\sigma| \ll 1$), mixing Eqs. (8) and (9) yields

$$-2\lambda N \sim (2-D) \int U|\phi|^2 d\vec{r} - \int U\vec{r} \cdot \vec{\nabla} |\phi|^2 d\vec{r}. \quad (69)$$

For a parabolic potential, $U = \Omega_0^2 r^2/4$, ground states with weak nonlinearity will thus preferably be associated with $\lambda < 0$. For the step potential (31), the same relation indicates that weak nonlinearities should rather concern the range $0 \leq \lambda \leq \epsilon$, if the inequality $R^D |\phi(R)|^2 \ll \int_0^R |\phi|^2 r^{D-1} dr$ holds.

Bound states in hollow capillaries can be treated through a similar analysis, as the boundary condition $\phi(r=R) = 0$ amounts to imposing walls at finite transverse radius in a Kerr medium. This meets an analogy with the properties of the former potentials. In this case again, the right qualitative behaviors of N_s vs λ are well restored by the variational method, provided that the test function includes a weight function making ϕ vanish at the finite boundary $r = R$. Applying *a priori* the criterion $d_\lambda N_s > 0$ for soliton stability, GS modes are stable in a focusing medium for small nonlinearities, when they adopt a distribution close to the fundamental Bessel mode $J_0(2.405r/R)$. Our analysis shows, however, that this Bessel shape holds in the limit of weak Kerr effect. For more intense beams with powers below the self-focusing

threshold, the stationary waveguides can still be stable, but their profile should resemble more the ground state of the unbounded NLS equation.

To the best of our knowledge, evidence of the stability of stationary soliton modes in 2D capillaries, for powers below the critical power for self-focusing, has not been presented before. We also investigated stability properties of singly charged and multicharged vortices in focusing media with a parabolic trap. As a result, we observed that vortex lines with unit charge ($|m|=1$) keep a robust shape, as long as their particle number remains below the threshold for collapse. Otherwise, they may decay into lower-order structures that eventually collapse in finite time. Multicharged vortices have been numerically shown to be unstable with attractive interactions. Depending on their initial number of particles, they

split into elementary vortices or break up into several spikes, which can collapse if their individual particle number is above critical.

In conclusion, the above-summarized variational procedure has systematically been applied to various inhomogeneities and trap potentials, both for focusing and defocusing media. It supplied reliable results compared with direct numerical integrations of Eq. (3). We believe that this method may successfully be applied to many other potentials belonging to the fields of nonlinear optics and of BEC physics.

ACKNOWLEDGMENTS

The authors thank R. Y. Chiao, J. Hickmann, and Yu. S. Kivshar for fruitful discussions.

-
- [1] A. C. Newell and J. V. Moloney, *Nonlinear Optics* (Addison-Wesley, Reading, MA, 1992).
- [2] A. Yariv, *Quantum Electronics*, 2nd ed. (Wiley, New York, 1975), p. 120.
- [3] L. Bergé, *Phys. Plasmas* **4**, 1227 (1997).
- [4] Yu. B. Gaididei, K. Ø. Rasmussen, and P. L. Christiansen, *Phys. Rev. E* **52**, 2951 (1995).
- [5] R. Y. Chiao, E. Garmire, and C. H. Townes, *Phys. Rev. Lett.* **13**, 479 (1964).
- [6] L. Bergé, *Phys. Rev. E* **62**, R3071 (2000).
- [7] H. A. Rose and M. I. Weinstein, *Physica D* **30**, 207 (1988).
- [8] N. G. Vakhitov and A. A. Kolokolov, *Radiophys. Quantum Electron.* **16**, 783 (1975); A. A. Kolokolov, *ibid.* **17**, 1016 (1976).
- [9] J. J. Rasmussen and K. Rypdal, *Phys. Scr.* **33**, 481 (1986).
- [10] Yu. B. Gaididei, J. Schjødt-Eriksen, and P. L. Christiansen, *Phys. Rev. E* **60**, 4877 (1999).
- [11] J. Schjødt-Eriksen, Yu. B. Gaididei, and P. L. Christiansen, *Phys. Rev. E* **64**, 066614 (2001).
- [12] J. T. Manassah, P. L. Baldeck, and R. R. Alfano, *Opt. Lett.* **13**, 589 (1988).
- [13] M. Karlsson, D. Anderson, and M. Desaix, *Opt. Lett.* **17**, 22 (1992).
- [14] J. T. Manassah, *Opt. Lett.* **17**, 1259 (1992).
- [15] G. Tempea and Th. Brabec, *Opt. Lett.* **23**, 762 (1998).
- [16] E. A. J. Marcetili and R. A. Schmelzter, *Bell Syst. Tech. J.* **43**, 1783 (1964).
- [17] F. Dorchies *et al.*, *Phys. Rev. Lett.* **82**, 4655 (1999).
- [18] G. Fibich and A. L. Gaeta, *Opt. Lett.* **25**, 335 (2000).
- [19] M. H. Anderson, J. R. Ensher, M. R. Matthews, C. E. Wieman, and E. A. Cornell, *Science* **269**, 198 (1995).
- [20] See for a review: F. Dalfovo, S. Giorgini, L. P. Pitaevskii, and S. Stringari, *Rev. Mod. Phys.* **71**, 463 (1999).
- [21] C. A. Sackett, J. M. Gerton, M. Welling, and R. G. Hulet, *Phys. Rev. Lett.* **82**, 876 (1999); J. M. Gerton, D. Strekalov, I. Prodan, and R. G. Hulet, *Nature (London)* **408**, 692 (2000).
- [22] Yu. S. Kivshar and T. J. Alexander, in *Yang-Baxter Systems, Nonlinear Models and Their Applications*, edited by B. K. Chung, Q. Han Park, and C. Rim (World Scientific, Singapore, 2000), pp. 98–115.
- [23] Yu. S. Kivshar, T. J. Alexander, and S. K. Turitsyn, *Phys. Lett. A* **278**, 225 (2001).
- [24] L. Bergé, T. J. Alexander, and Yu. S. Kivshar, *Phys. Rev. A* **62**, 023607 (2000).
- [25] R. Y. Chiao, *Opt. Commun.* **179**, 157 (2000).
- [26] E. L. Bolda, R. Y. Chiao, and W. H. Zurek, *Phys. Rev. Lett.* **86**, 416 (2001).
- [27] J. Boyce, J. P. Torres, and R. Y. Chiao, *Opt. Lett.* **24**, 1850 (1999).
- [28] E. A. Kuznetsov and J. J. Rasmussen, *Phys. Rev. E* **51**, 4479 (1995).
- [29] I. V. Barashenkov, *Phys. Rev. Lett.* **77**, 1193 (1996).
- [30] V. I. Kruglov and R. A. Vlasov, *Phys. Lett. A* **111**, 401 (1985).
- [31] J. Atai, Y. Chen, and J. M. Soto-Crespo, *Phys. Rev. A* **49**, R3170 (1994); J. M. Soto-Crespo *et al.*, *ibid.* **44**, 636 (1991).
- [32] W. J. Firth and D. V. Skryabin, *Phys. Rev. Lett.* **79**, 2450 (1997); D. V. Skryabin, *Phys. Rev. A* **63**, 013602 (2001).
- [33] V. Tikhonenko, J. Christou, and B. Luther-Davies, *Phys. Rev. Lett.* **76**, 2698 (1996).
- [34] A. V. Mamaev, M. Saffman, and A. A. Zozulya, *Phys. Rev. Lett.* **78**, 2108 (1997).
- [35] A. V. Mamaev, A. A. Zozulya, V. K. Mezentsev, D. Z. Anderson, and M. Saffman, *Phys. Rev. A* **56**, R1110 (1997).
- [36] Yu. S. Kivshar and B. Luther-Davies, *Phys. Rep.* **298**, 81 (1998).
- [37] G. Baym and C. J. Pethick, *Phys. Rev. Lett.* **76**, 6 (1996); see also E. Lundh, C. J. Pethick, and H. Smith, *Phys. Rev. A* **55**, 2126 (1997).
- [38] R. J. Dodd, K. Burnett, M. Edwards, and C. W. Clark, *Phys. Rev. A* **56**, 587 (1997).
- [39] A. A. Svidzinsky and A. L. Fetter, *Phys. Rev. A* **58**, 3168 (1998); *Phys. Rev. Lett.* **84**, 5919 (2000); see also D. S. Rokhsar, *ibid.* **79**, 2164 (1997).
- [40] Y. Castin and R. Dum, *Eur. Phys. J. D* **7**, 399 (1999).
- [41] H. Pu, C. K. Law, J. H. Eberly, and N. P. Bigelow, *Phys. Rev. A* **59**, 1533 (1999).
- [42] P. O. Fedichev and G. V. Shlyapnikov, *Phys. Rev. A* **60**, R1779 (1999).
- [43] M. R. Matthews, B. P. Anderson, P. C. Haljan, D. S. Hall, C. E. Wieman, and E. A. Cornell, *Phys. Rev. Lett.* **83**, 2498 (1999).

- [44] K. W. Madison, F. Chevy, W. Wohlleben, and J. Dalibard, Phys. Rev. Lett. **84**, 806 (2000); F. Chevy, K. W. Madison, and J. Dalibard, *ibid.* **85**, 2223 (2000).
- [45] O. M. Maragò, S. A. Hopkins, J. Arlt, E. Hodby, G. Hechenblaikner, and C. J. Foot, Phys. Rev. Lett. **84**, 2056 (2000).
- [46] E. L. Bolda and D. F. Walls, Phys. Rev. Lett. **81**, 5477 (1998).
- [47] F. Chevy, K. W. Madison, V. Bretin, and J. Dalibard, Phys. Rev. A **64**, 031601(R) (2001).
- [48] B. Jackson, J. F. McCann, and C. S. Adams, Phys. Rev. Lett. **80**, 3903 (1998).
- [49] C. Raman, K. Köhl, R. Onofrio, D. S. Durfee, C. E. Kuklewicz, Z. Hadzibabic, and W. Ketterle, Phys. Rev. Lett. **83**, 2502 (1999); R. Onofrio, C. Raman, J. M. Vogels, J. R. Abo-Shaer, A. P. Chikkatur, and W. Ketterle, *ibid.* **85**, 2228 (2000).
- [50] T. Frisch, Y. Pomeau, and S. Rica, Phys. Rev. Lett. **69**, 1644 (1992).
- [51] A. P. Chikkatur, A. Görlitz, D. M. Stamper-Kurn, S. Inouye, S. Gupta, and W. Ketterle, Phys. Rev. Lett. **85**, 483 (2000).
- [52] S. Burger, K. Bongs, S. Dettmer, W. Ertmer, K. Sengstock, A. Sanpera, G. V. Shlyapnikov, and M. Lewenstein, Phys. Rev. Lett. **83**, 5198 (1999).
- [53] A. E. Muryshev, H. B. van Linden van den Heuvell, and G. V. Shlyapnikov, Phys. Rev. A **60**, R2665 (1999); P. O. Fedichev, A. E. Muryshev, and G. V. Shlyapnikov, *ibid.* **60**, 3220 (1999).
- [54] D. Anderson, M. Bonnedal, and M. Lisak, Phys. Fluids **22**, 1838 (1979).
- [55] M. I. Weinstein, Commun. Math. Phys. **87**, 567 (1983).
- [56] K. Rypdal, J. J. Rasmussen, and K. Thomsen, Physica D **16**, 339 (1985).
- [57] E. A. Kuznetsov, J. J. Rasmussen, K. Rypdal, and S. K. Turitsyn, Physica D **87**, 273 (1995).
- [58] M. Desaix, D. Anderson, and M. Lisak, J. Opt. Soc. Am. B **8**, 2082 (1991).
- [59] Y. Chen, IEEE J. Quantum Electron. **27**, 1236 (1991).
- [60] V. I. Kruglov, V. M. Volkov, R. A. Vlasov, and V. V. Drits, J. Phys. A: Math. Gen. **21**, 4381 (1988); V. I. Kruglov, Yu. A. Logvin, and V. M. Volkov, J. Mod. Opt. **39**, 2277 (1992).